

Galactic Chemical Evolution and solar *s*-process abundances: dependence on the ^{13}C -pocket structure

S. Bisterzo¹ and C. Travaglio²

INAF - Astrophysical Observatory Turin, Turin, Italy

bisterzo@to.infn.it; sarabisterzo@gmail.com

R. Gallino²

Department of Physics, University of Turin, Italy

M. Wiescher

Joint Institute for Nuclear Astrophysics (JINA), Department of Physics, University of
Notre Dame, IN, USA

and

F. Käppeler

Karlsruhe Institute of Technology, Campus Nord, Institut für Kernphysik, Karlsruhe,
Germany

Received _____; accepted _____

¹Department of Physics, University of Turin, Italy

²B2FH Association-c/o Strada Osservatorio 20, 10023 Turin, Italy

ABSTRACT

We study the s -process abundances ($A \gtrsim 90$) at the epoch of the solar-system formation. AGB yields are computed with an updated neutron capture network and updated initial solar abundances. We confirm our previous results obtained with a Galactic Chemical Evolution (GCE) model: (i) as suggested by the s -process spread observed in disk stars and in presolar meteoritic SiC grains, a weighted average of s -process strengths is needed to reproduce the solar s -distribution of isotopes with $A > 130$; (ii) an additional contribution (of about 25%) is required in order to represent the solar s -process abundances of isotopes from $A = 90$ to 130.

Furthermore, we investigate the effect of different internal structures of the ^{13}C -pocket, which may affect the efficiency of the $^{13}\text{C}(\alpha, n)^{16}\text{O}$ reaction, the major neutron source of the s -process. First, keeping the same ^{13}C profile adopted so far, we modify by a factor of two the mass involved in the pocket; second, we assume a flat ^{13}C profile in the pocket, and we test again the effects of the variation of the mass of the pocket.

We find that GCE s -predictions at the epoch of the solar-system formation marginally depend on the size and shape of the ^{13}C -pocket once a different weighted range of ^{13}C -pocket strengths is assumed. We ascertain that, independently of the internal structure of the ^{13}C -pocket, the missing solar-system s -process contribution in the range from $A = 90$ to 130 remains essentially the same.

Subject headings: Stars: AGB – Stars, chemical evolution – Galaxy

1. Introduction

The solar-system abundances result from contributions of different nucleosynthesis processes. Isotopes heavier than the iron group are produced via neutron captures, the *slow* and the *rapid* processes (*s* and *r*). Exceptions include the 35 or so¹ isotopes synthesized by the *p*-process.

The origin of the *r*-process is currently attributed to explosive nucleosynthesis in massive stars, even if the astrophysical conditions are still not well defined (see, e.g., Thielemann et al. 2011). The *p*-process is identified with photo-disintegration processes (the so-called γ -process; Howard, Meyer, & Woosley 1991) of heavy elements occurring in core collapse Supernovae of Type II (e.g., Rauscher et al. 2002; Hayakawa et al. 2008). Accreting white dwarfs in binary systems with masses approaching the Chandrasekhar limit may substantially contribute to the production of *p*-process nuclei when they explode as Type Ia Supernovae (e.g., Travaglio et al. 2011, and references therein).

Concerning the *s*-process, pioneering studies (Seeger, Fowler, & Clayton 1965; Clayton & Rassbach 1967) have demonstrated that the solar *s*-distribution of isotopes from iron to bismuth may be reproduced by three components: the *weak*, the *main* and the *strong* component. The *weak* component contributes to *s*-isotopes up to $A \sim 90$. It takes place in massive stars during core He and convective shell C burning (see, e.g., Pignatari et al. 2010; Frischknecht, Hirschi, & Thielemann 2012). The *main* component ($A \sim 90$ to 208) derives from low mass asymptotic giant branch (AGB) stars, during their thermally pulsing (TP) phase (Arlandini et al. 1999; Goriely & Mowlavi 2000; Cristallo et al. 2009; Bisterzo et al. 2011; Lugaro et al. 2012). The *strong* component is needed to reproduce about half of solar ²⁰⁸Pb. It originates from AGB stars of low

¹The original 35 proton-rich nuclei reported by Cameron (1957) and Burbidge et al. (1957) were defined on the basis of being apparently excluded by the *s*- or by the *r*-process.

metallicity (at $[\text{Fe}/\text{H}] \sim -1$; Gallino et al. 1998; Travaglio et al. 2001; Van Eck et al. 2001).

After a limited number of TPs, at the quenching of recurrent thermal instabilities in the He shell, the convective envelope penetrates in the outer region of the He-intershell (third-dredge-up, TDU), bringing to the surface newly synthesized ^{12}C and *s*-process isotopes. The whole envelope undergoes strong mass loss by stellar winds, leaving the degenerate core that eventually will become a white dwarf.

The major neutron source of the *s*-process in low mass AGB stars ($M < 4 M_{\odot}$) is the $^{13}\text{C}(\alpha, n)^{16}\text{O}$ reaction, which is activated in radiative conditions during the interpulse phase (Straniero et al. 1995). At the quenching of a TDU, a small amount of hydrogen is assumed to penetrate from the envelope into the top layers of the radiative He-rich zone. At hydrogen re-ignition, a thin ^{13}C -pocket forms by proton captures on the abundant ^{12}C . When the temperature of $\sim 9 \times 10^7$ K is reached (which corresponds to $kT \sim 8$ keV), ^{13}C is fully depleted releasing neutrons with a density of about 10^7 n/cm $^{-3}$.

The ^{13}C in the pocket is of primary origin, directly synthesized in the star from the ^{12}C produced by partial He burning during previous thermal pulse and is independent of the initial composition. However, the number of free neutrons per iron seed increases with decreasing metallicity. Consequently, for a given ^{13}C -pocket strength, the *s*-process flow firstly feeds the *s*-process peak Sr-Y-Zr (at magic neutron number $N = 50$), extending up to ^{136}Ba , then reaches the second *s*-process peak (Ba-La-Pr-Ce-Nd at $N = 82$), extending up to ^{204}Pb - ^{207}Pb , with a progressive increasing ratio of the heavy-*s* elements (hs) to the light-*s* elements (ls). At even lower metallicity, it mainly feeds ^{208}Pb ($N = 126$) at the termination of the *s*-process path. Therefore, the *s*-process in AGB stars is strongly metallicity dependent. The complexity of the *s*-process distribution in AGB stars is confirmed by spectroscopic observations in different stellar populations (planetary nebulae, post-AGB, MS, S, C(N), Ba, CH and CEMP-*s* stars; see, e.g., Smith & Lambert 1990; Péquignot & Baluteau 1994; Aoki et al. 2002; Abia et al. 2002; Allen & Barbuy

2006; Jonsell et al. 2006; Sharpee et al. 2007; Sterling & Dinerstein 2008; Reyniers et al. 2007; Zamora et al. 2009). Furthermore, for a given metallicity a spread in the s -process distribution is observed for each class of stars. A range of ^{13}C -pocket strengths is needed in order to explain this spread (see, e.g., Busso et al. 2001; Sneden, Cowan & Gallino 2008; Käppeler et al. 2011; Bisterzo et al. 2011; Lugaro et al. 2012). A similar spread is shown by s -process isotopic signatures found in presolar meteoritic SiC grains, which originated in the outflow of AGB stars (see, e.g., Lugaro et al. 2003; Clayton & Nittler 2004; Zinner 2007).

A marginal activation of the $^{22}\text{Ne}(\alpha, n)^{25}\text{Mg}$ reaction occurs at the bottom of the advanced convective thermal pulses, where a temperature of $T \sim 3 \times 10^8$ K is reached. A short neutron burst is released with a peaked neutron density (up to $N_n \sim 10^{11}$ n/cm $^{-3}$), which provides only a few percent of the total neutron exposure, but affects the abundances of some important isotopes close to the main branchings of the s -process (e.g., ^{85}Kr and ^{95}Zr , sensitive to neutron density).

For an extended review on the s -process we refer to Käppeler et al. (2011), and references therein.

Several model uncertainties affect the AGB yields, e.g., the mass loss efficiency, the deepness of the TDU, and the number of TPs (Herwig 2005; Straniero, Gallino & Cristallo 2006). Particularly challenging in AGB modeling is the formation of the ^{13}C -pocket and the physical prescriptions involved. Iben & Renzini (1983) suggested that, as a consequence of the TDU, a sharp discontinuity between the H-rich envelope and the He- and C-rich intershell forms, and a partial mixing of protons from the envelope into the He-intershell may take place. The amount of protons that diffuses into the He-intershell must be small to allow the production of ^{13}C and to limit the further conversion of ^{13}C to ^{14}N by proton captures. ^{14}N mainly acts as a neutron poison of the s -process via the $^{14}\text{N}(n, p)^{14}\text{C}$ reaction. In the external zone of the pocket (where protons are more abundant), a ^{14}N -rich zone may

also form, depending on the proton profile adopted in the AGB model; this region plays a minor role in the *s*-process nucleosynthesis.

The hydrogen profile and, correspondingly, the internal structure of the ^{13}C -pocket may depend on the initial mass and metallicity of the AGB, and on the physical mechanisms that may compete inside the star itself. Herwig et al. (1997) proposed an exponential diffusive overshooting at the borders of all convective zones. FRUITY models by Cristallo et al. (2009, 2011) adopted an opacity-induced overshooting at the base of the convective envelope by introducing in the model an exponentially decaying profile of the convective velocity. Starting from Langer et al. (1999), Herwig, Langer & Lugaro (2003) and Siess, Goriely, & Langer (2004), rotation was introduced in stellar models to study its impact on the ^{13}C -pocket structure. First studies agree that rotation-induced instabilities reduce the total mass of ^{13}C in the pocket, owing to the ^{14}N contamination in the ^{13}C -rich layer, compromising the *s*-process efficiency. Piersanti, Cristallo, & Straniero (2013) confirm that rotation-induced instabilities modify the mass extension of both ^{13}C and ^{14}N abundances in the pocket, and their overlap as well. Moreover, they suggest that meridional (Eddington-Sweet) circulation may smooth and enlarge the ^{13}C -rich zone of the pocket.

Denissenkov & Tout (2003) demonstrated that a weak turbulence induced by gravity waves presents additional alternative for the ^{13}C -pocket formation. On the other hand, Busso et al. (2012) revisit the idea that rotation favors mixing indirectly, through the maintenance of magnetic dynamo mechanisms, producing the buoyancy of toroidal magnetic structures (Busso et al. 2007).

Further investigations on rotation, magnetic fields, gravity waves and the interplay between these several mechanisms will help to shed light on this challenging issue.

The solar system *s*-process distribution is the result of the nucleosynthesis of all previous generations of AGB stars that have polluted the interstellar medium. Therefore, a Galactic chemical evolution (GCE) model is required to follow the complex evolutionary

processes of the Milky Way. Travaglio et al. (1999) showed that AGB yields computed within a weighted average over the range of ^{13}C -pockets are needed in the framework of GCE model to reproduce the s -distribution observed in the solar system. This is also suggested by the spectroscopic s -process spread observed in individual stars and the isotopic anomalies measured in presolar SiC grains.

GCE calculations succeeded to reproduce the solar abundances of s -only isotopes between ^{134}Ba and ^{208}Pb (Travaglio et al. 2001, 2004). However, a deficit (of about 25%) between GCE predictions at the solar epoch and the abundances measured in the solar system was found for Sr, Y, Zr, and s -process isotopes up to $A = 130$, including ten s -only isotopes from ^{96}Mo to ^{130}Xe (see also Käppeler et al. 2011; their Fig. 15). The *weak* – s process produces isotopes up to Sr ($\sim 10\%$ to Sr and $\lesssim 5\%$ to Y and Zr isotopes), with a negligible contribution afterwards. An additional r -fraction of $\sim 10\%$ was estimated for solar Sr-Y-Zr, evaluating the r -contribution from the prototypical r-II star CS 22892–052². Summing up, the s -, r - (and p -) contributions predicted by current stellar models are not sufficient to explain the solar abundances of light isotopes from $A \sim 90$ to 130. Travaglio et al. (2004) hypothesized the existence of an additional process of unknown origin, called by the authors LEPP (light-element primary process), which must supply $\sim 8\%$ of solar Sr and $\sim 18\%$ of solar Y and Zr. Several scenarios have been recently explored, involving a primary component in massive stars that comes from the activation of $^{13}\text{C}(\alpha, n)^{16}\text{O}$ in the C core when the temperature is low enough to prevent the $^{13}\text{N}(\gamma, p)^{12}\text{C}$ reaction from becoming efficient (defined "cold" C-burning component or *cs*-component by Pignatari et al. 2013), and/or a light r -process induced by explosive stellar nucleosynthesis, e.g., in the neutrino-driven winds (Arcones & Thielemann 2013 and references therein).

²CS 22892–052 has an r -process enrichment of ~ 40 times the solar-scaled composition ($[\text{Eu}/\text{Fe}] = 1.6$; Sneden et al. 2003).

The aim of this work is to investigate the influence of one of the major AGB yield uncertainties, the formation of the ^{13}C -pocket, on the predicted solar s -process distribution, from light neutron capture isotopes (to verify the need of LEPP) up to Pb and Bi at the end of the s -path. Firstly, in Section 2 we present updated s -percentages for isotopes from Kr to Bi with respect to Travaglio et al. (2004). In Section 3, we test the effect of AGB yields computed with different choices of the internal structure of the ^{13}C -pocket on GCE s -predictions at the epoch of the solar-system formation. Our results are briefly summarized in Section 4.

2. Updated solar s -abundances predicted by GCE

2.1. The Galactic chemical evolution model

The general structure of the Galactic chemical evolution (GCE) model adopted in this work is the same described by Travaglio et al. (2004). The GCE model follows the composition of stars, stellar remnants, interstellar matter (atomic and molecular gas), and their mutual interaction, in the three main zones of the Galaxy, halo, thick disk, and thin disk. We concentrate on the chemical evolution inside the solar annulus, located 8.5 kpc from the Galactic center. The thin disk is divided into independent concentric annuli, and we neglect any dependence on Galactocentric radius.

The chemical evolution is regulated by the star formation rate (SFR), initial mass function (IMF), and nucleosynthesis yields from different stellar mass ranges and populations. The star formation rate has been determined self-consistently as the result of aggregation, interacting and interchanging processes of the interstellar gas, which may occur spontaneously or stimulated by the presence of other stars. The stellar contributions from different mass ranges, or from single and binary stars are treated separately: we distinguish between single low- and intermediate-mass stars ending their life as a He or C-O white

dwarf ($0.8 M_{\odot} \leq M < 8 M_{\odot}$), single massive stars exploding as Type II supernovae (SNeII, $8 M_{\odot} \leq M \leq 100 M_{\odot}$), and binary stars that give rise to Type Ia supernova (SNIa) events. SFR and IMS are the same adopted by Travaglio et al. (2004).

In Fig. 1 (*top panel*), the SFR rate in the three Galactic zones is displayed versus [Fe/H]. Galactic halo and thick disk are assumed to form on a relatively short time scale: after only <0.5 Gyr the metallicity increases up to $[\text{Fe}/\text{H}] \sim -1.5$ (halo phase), to reach $[\text{Fe}/\text{H}] \sim -1.0$ faster than in 2 Gyr. The thin-disk phase in our GCE model starts after ~ 1 Gyr, at $[\text{Fe}/\text{H}] \sim -1.5$. The corresponding [O/Fe] versus [Fe/H] is shown in Fig. 1 (*bottom panel*), together with an updated compilation of observational data (see caption). Because oxygen is mainly synthesized by short-lived SNeII, and under the hypothesis that Fe is mostly produced by long-lived SNeIa ($\sim 1/3$ by SNeII and $\sim 2/3$ by SNeIa), the presence of a knee in the trend of [O/Fe] vs [Fe/H] indicates the delayed contribution to iron by SNeIa. We refer to Travaglio et al. (2004) (and references therein), for more details on the adopted GCE model.

The Galactic chemical evolution is computed as function of time up to the present epoch ($t_{\text{Today}} = 13.8$ Gyr, updated by WMAP; Spergel et al. 2003; Bennett et al. 2013). Given that the solar system formation occurred 4.6 Gyr ago, the Galactic time corresponding to the birth of the solar system is $t_{\odot} = 9.2$ Gyr, about 0.7 Gyr later than found by Travaglio et al. (2004). This temporal shift has been achieved by slightly reducing the Fe contribution by SNeIa.

Solar abundances have been updated according to Lodders, Palme & Gail (2009), while Travaglio et al. (2004) adopted solar values by Anders & Grevesse (1989).

Stellar yields by Rauscher et al. (2002) and Travaglio et al. (2004a) are used for SNeII and SNeIa, respectively. A detailed description of the AGB yields adopted in this work is given in Section 2.2.

2.2. The AGB yields

We have considered a set of five AGB models with low initial mass ($M = 1.3, 1.4, 1.5, 2,$ and $3 M_{\odot}$, representing the AGB mass range $1.3 \leq M/M_{\odot} < 4$; hereafter LMS) and two AGB models with intermediate initial mass ($M = 5$ and $7 M_{\odot}$, among $4 \leq M/M_{\odot} < 8$; hereafter IMS).

The s -process AGB yields have been obtained with a post-process nucleosynthesis method (Gallino et al. 1998) based on input data (like temperature and density during TPs, the mass of the H-shell and He-intershell, the overlapping factor and the residual mass of the envelope) of full evolutionary FRANEC models by Straniero et al. (2003) for LMS and Straniero et al. (2000) for IMS. For details on AGB models we refer to Bisterzo et al. (2010). Here we briefly review the basic information useful to this work.

As described in Section 1, the total mass of the pocket and the ^{13}C and ^{14}N profiles inside the pocket itself are not well established, owing to the lack of a definite description of the physical mechanisms that allow the diffusion of a few protons into the He intershell. In our LMS models, the amount of ^{13}C and ^{14}N in the ^{13}C -pocket are artificially introduced. The ^{13}C and ^{14}N abundances, are treated as free parameters kept constant pulse by pulse. We adopt a specific shape and size of the ^{13}C -pocket called case ST (see Section 3), which was used to reproduce the solar *main* component of the s -process as the average of two AGB models with initial mass $M = 1.5$ and $3.0 M_{\odot}$ and half solar metallicity (see Arlandini et al. 1999).

To interpret the spectroscopic s -process spread observed in C and s -rich stars at a given metallicity, LMS models are computed for a large range of ^{13}C -pockets, obtained by multiplying or dividing the ^{13}C (and ^{14}N) abundances of case ST by different factors, and leaving the mass of the pocket constant. The case ST \times 2 corresponds to an upper limit, because further proton ingestion leads to the formation of ^{14}N at expenses of ^{13}C . The

minimum ^{13}C -pocket that significantly affects the s -distribution depends on the initial iron content of the star, given that the number of neutrons available per iron seeds increases with decreasing metallicity. As minimum ^{13}C -pocket, we assume case ST \times 0.1 at disk metallicities and case ST \times 0.03 in the halo (see discussion by Bisterzo et al. 2010, 2011).

LMS models of $M = 1.3, 1.4, 1.5$ and $2 M_{\odot}$ have been computed following the interpolation formulae given by Straniero et al. (2003) for $-1.0 \leq [\text{Fe}/\text{H}] \leq 0.0$, and then further extrapolating the stellar parameters from $[\text{Fe}/\text{H}] = +0.2$ down to $[\text{Fe}/\text{H}] = -3.6$ as described by Bisterzo et al. (2010). Note that for $M = 1.3 M_{\odot}$ models the conditions for the activation of the TDU episodes are never reached for metallicities higher than $[\text{Fe}/\text{H}] \sim -0.6$ (Straniero et al. 2003), and we compute $1.3 M_{\odot}$ yields starting from $[\text{Fe}/\text{H}] = -0.6$ down to -3.6 .

Starting from Domínguez et al. (1999) (see also Boothroyd & Sackmann 1988), it was shown that, for a given initial mass, the core mass increases with decreasing metallicity and AGB models with $M \gtrsim 3 M_{\odot}$ and $[\text{Fe}/\text{H}] \sim -1.3$ are not far from the transition zone between LMS and IMS stars. As discussed by Bisterzo et al. (2010), we have assumed that AGB stars with $M = 3 M_{\odot}$ should behave as IMS for $[\text{Fe}/\text{H}] \lesssim -1.6$. Thus, our $3 M_{\odot}$ models have been computed by extrapolating the stellar parameters from $3 M_{\odot}$ models by Straniero et al. (2003) in the metallicity interval between $-1.6 \leq [\text{Fe}/\text{H}] \leq +0.2$.

We recall that low metallicity IMS stars may be affected by an extremely efficient dredge-up called hot TDU (Herwig 2004; Lau, Stancliffe, & Tout 2009), which may influence the structure of the star and its evolution. Because nucleosynthesis models which include hot TDU are still subject of study, we have computed IMS yields only for $[\text{Fe}/\text{H}] \geq -1.6$ (Bisterzo et al. 2010).

IMS models are based on full evolutionary AGB models by Straniero et al. (2000). Their $5.0 M_{\odot}$ models at $[\text{Fe}/\text{H}] = 0$ and -1.3 show comparable characteristics, e.g.,

temperature during TPs, TDU and He-intershell masses. Thus, we have assumed that the structure of $5.0 M_{\odot}$ models from $[\text{Fe}/\text{H}] = +0.2$ down to $[\text{Fe}/\text{H}] = -1.6$ are barely distinguishable from solar. Solar 5 and $7 M_{\odot}$ models described by Straniero et al. (2000) have comparable He-intershell mass and temperature at the bottom of the TPs, while the TDU mass is a factor of ~ 6 lower in $7 M_{\odot}$ model. Starting from these stellar characteristics, we have extrapolated the $7.0 M_{\odot}$ models in the metallicity range between $-1.6 \leq [\text{Fe}/\text{H}] \leq +0.2$.

The treatment of mass loss in IMS models is largely uncertain (see, e.g., Ventura & D’Antona 2005a), and the number of TPs with TDU experienced by IMS stars may vary by a factor of three or more, affecting the structure and nucleosynthesis of the star itself. With the efficient mass loss adopted in our IMS models, AGB with $M = 5$ and $7 M_{\odot}$ experience 24 TPs followed by TDU (Bisterzo et al. 2010).

IMS AGB stars play a minor role in the Galactic enrichment of s -process isotopes, with the exception of a few neutron-rich isotopes as ^{86}Kr , ^{87}Rb , and ^{96}Zr (Travaglio et al. 2004). Indeed, the mass of the He-intershell is about a factor of ten lower in IMS than in LMS. Thus, the overall amount of material dredged into the envelope of IMS decreases by at least one order of magnitude with respect to LMS (Straniero et al. 2000). Moreover, IMS experience hot bottom burning during the interpulse phase: the bottom of the convective envelope reaches the top of the H-burning shell and the temperature at the base is large enough ($T \gtrsim 4 \times 10^7$ K) to activate the CN cycle, thus converting ^{12}C to ^{14}N (see, e.g., Karakas & Lattanzio 2003; Ventura & D’Antona 2005). Hot bottom burning may even inhibit the formation of the ^{13}C -pocket in IMS of low metallicity (Goriely & Siess 2004; Herwig 2004). As a consequence, the $^{13}\text{C}(\alpha, n)^{16}\text{O}$ neutron source is expected to have a small or even negligible effect on neutron capture isotopes heavier than $A \sim 90$. Based on these considerations, new AGB IMS yields have been computed with a negligible ^{13}C -pocket. The introduction of a small ^{13}C -pocket ($M(^{13}\text{C}) = 10^{-7} M_{\odot}$), as assumed

in the old IMS models adopted by Travaglio et al. (2004), has negligible effects on solar *s*-process predictions (see Section 2.3).

On the other hand, a higher temperature is reached at the bottom of the TPs of IMS ($T \sim 3.5 \times 10^8$ K), so that the $^{22}\text{Ne}(\alpha, n)^{25}\text{Mg}$ reaction is efficiently activated. Because of the high peak neutron density ($N_n \sim 10^{12}$ n/cm⁻³), ^{86}Kr , ^{87}Rb , and ^{96}Zr are strongly overproduced, owing to the branchings at ^{85}Kr , ^{86}Rb and ^{95}Zr . The observational evidence of the strong activation of the $^{22}\text{Ne}(\alpha, n)^{25}\text{Mg}$ reaction (associated to IMS) is the excess of Rb with respect to Zr (see, e.g., Lambert et al. 1995; Tomkin & Lambert 1999; Abia et al. 2001, and the most recent Yong et al. 2008; García-Hernández et al. 2009, 2013; D’Orazi et al. 2013). The high [Rb/Zr] observed in some OH/IR AGB stars seems to be incompatible with IMS predictions. Karakas, García-Hernández, & Lugaro (2012) proposed that delayed superwinds may increase the number of TPs, and thus, the [Rb/Fe] and [Rb/Zr] predictions. A complementary possibility to solve the mismatch between observed and predicted [Rb/Zr] in OH/IR AGB stars has been suggested by García-Hernández et al. (2009) and van Raaij et al. (2012), who discussed how model atmospheres of luminous pulsating AGB stars may be incomplete³ and [Rb/Fe] may be overestimated.

Given the present uncertainties, our 5 and 7 M_{\odot} models may experience a larger number of TPs under the hypothesis of a less efficient mass loss. However, the resulting effect on solar *s*-process predictions is marginal (with the exception of the neutron-rich isotopes ^{86}Kr , ^{87}Rb , and ^{96}Zr , see Section 2.3), because the solar *s*-contribution from LMS stars dominates over IMS.

In IMS with initial mass of $M \sim 6$ to $8 M_{\odot}$, the temperature at the base of the convective envelope further increases ($T \gtrsim 1 \times 10^8$ K), leading to a greater degree of

³E.g., circumstellar dust envelope and dust formation, and 3D hydrodynamical simulations are not included; NLTE effects are not considered.

proton-capture nucleosynthesis that efficiently activates CNO, NeNa and MgAl cycles as well. These more massive AGB stars, ending as Ne-O core white dwarfs or possibly less massive neutron stars, are called super-AGB stars (SAGB). The mass and metallicity limits of SAGB depend on models, and the treatment of core carbon ignition and burning and the efficiency of the TDU is very uncertain (e.g., Siess 2010; Ventura et al. 2013). At present, SAGB yields have not been included in our GCE calculations because no information about heavy *s*-process elements is available in literature (Karakas, García-Hernández, & Lugaro 2012; Doherty et al. 2014).

About fourteen hundred AGB models with initial masses $M = 1.4, 1.5, 2 M_{\odot}$ have been computed in the metallicity range between $[\text{Fe}/\text{H}] = -3.6$ up to $+0.2$, for a range of ^{13}C -pockets and a total of twenty-eight metallicities. About three hundred AGB models with initial masses $M = 1.3 M_{\odot}$ have been computed between $[\text{Fe}/\text{H}] = -3.6$ up to -0.6 , for a range of ^{13}C -pockets and a total of twenty metallicities. Note that the *s*-process abundances in the interstellar medium at the epoch of the solar system formation essentially derive from previous AGB generations starting from $[\text{Fe}/\text{H}] \gtrsim -1.6$ (see Travaglio et al. 2004; Serminato et al. 2009). Thus, AGB models with a more refined grid of twenty metallicities have been computed between $[\text{Fe}/\text{H}] = -1.6$ and 0 .⁴ Similarly, about three hundred $3 M_{\odot}$ models have been run between $[\text{Fe}/\text{H}] = -1.6$ up to $+0.2$, for a range of ^{13}C -pockets and a total of twenty metallicities. Forty $M = 5$ and $7 M_{\odot}$ models with a negligible ^{13}C -pocket have been calculated between $[\text{Fe}/\text{H}] = -1.6$ up to $+0.2$, for twenty metallicities in total.

Linear interpolations/extrapolations over the whole mass AGB range ($1.3 \leq M/M_{\odot} < 8$, with mass steps of $0.1 M_{\odot}$) have been carried out for AGB yields not explicitly calculated. With respect to Travaglio et al. (2004), we have introduced new AGB models of initial

⁴Twelve metallicities between $[\text{Fe}/\text{H}] = -1.6$ and -0.6 have been run for $1.3 M_{\odot}$ models.

masses 1.3, 1.4 and 2 M_{\odot} .

All AGB yields have been computed with an updated neutron capture network according to the online database KADoNiS⁵, and more recent measurements: $^{92,94,96}\text{Zr}$ (Tagliente et al. 2010, 2011,a), $^{186,187,188}\text{Os}$ (Mosconi et al. 2010), the p-only ^{180}W (Marganiec et al. 2010), as well as ^{41}K and ^{45}Sc (Heil et al. 2009), $^{24,25,26}\text{Mg}$ (Massimi et al. 2012), ^{63}Ni (Lederer et al. 2013), $^{64,70}\text{Zn}$ (Reifarth et al. 2012), among light isotopes that marginally affect the s-process contribution. Note that we employed Mutti et al. (2005) for $^{80,82,83,84,86}\text{Kr}$, Patronis et al. (2004) for $^{136,137}\text{Cs}$, Reifarth et al. (2003) for $^{148,149}\text{Pm}$ and Best et al. (2001) for $^{152,154}\text{Eu}$. Furthermore, AGB initial abundances are scaled to the updated solar values by Lodders, Palme & Gail (2009).

2.3. Discussion of the results

The s-process GCE predictions at the epoch of the solar system formation are displayed in Fig. 2 as percentages of the abundances by Lodders, Palme & Gail (2009). The s-only isotopes are represented by solid circles. Different symbols have been used for ^{96}Zr (big asterisk), ^{180}Ta (empty circle), which also receives contributions from the p process and from neutrino-nucleus interactions in massive stars, and ^{187}Os (empty triangle), which is affected by the long-lived decay of ^{187}Re (4.1×10^{10} yr). We distinguish ^{208}Pb , which is produced at $\sim 50\%$ by LMS of low metallicity, with a big filled square.

In the framework of GCE we have considered a weighted average among the various ^{13}C -pocket strengths (see Section 1). Observations of s-process rich stars at disk metallicity

⁵Karlsruhe Astrophysical Data Base of Nucleosynthesis in Stars, web site <http://www.kadonis.org/>; version v0.3.

(see, e.g., Käppeler et al. 2011, their Fig. 12) suggest that most of them lie in the range between case $ST \times 1.5$ down to $ST/1.5$. Very few stars can be interpreted by case $ST \times 2$. Actually, for ^{13}C -pockets below case $ST/6$ the s -enhancement becomes negligible. We exclude case $ST \times 2$ from the average of the ^{13}C -pockets, and we give a weight of $\sim 25\%$ to case $ST \times 1.3$. The unbranched s -only ^{150}Sm can be taken as reference isotope for the whole s -process distribution, because its solar abundance is well defined (5% uncertainty as a rare earth element, "REE") and the neutron capture cross section is given at 1%.

A complete list of s -process percentages of all isotopes and elements from Kr to Bi is given in Table 1, where updated GCE results are compared with previous GCE predictions by Travaglio et al. (2004). The theoretical s -process predictions by Travaglio et al. (2004) were normalized to solar abundances by Anders & Grevesse (1989). The s -percentages of LMS, IMS and the total s -contribution (LMS + IMS) are reported for GCE results by Travaglio et al. (2004) (columns 3, 4 and 5) and this work (columns 6, 7 and 8). Values in column 8 correspond to those displayed in Fig. 2. In comparison to GCE results, we list in column 2 the *main* – s process contributions by Bisterzo et al. (2011), obtained as in Arlandini et al. (1999) by averaging between AGB models of $M = 1.5$ and $3 M_{\odot}$ and half solar metallicity.

The variations between GCE results by Travaglio et al. (2004) and those computed in this work (see Table 1) are partly due to the updated nuclear reaction network and new solar abundances.

The solar abundance distribution is essentially based on CI carbonaceous chondrite measurements in terrestrial laboratories with increasingly accurate experimental methods. Among the exceptions are volatile elements as CNO, which are evaluated from photospheric determinations, or noble gases as Ne, evaluated from solar corona winds. Kr and Xe solar abundances are derived theoretically from neutron-capture element systematics

(Palme & Beer 1993; Reifarth et al. 2002). Since 1989, C, N and O abundances have been steadily revised downward thanks to progress in atmospheric models (see, e.g., Asplund 2005), partially affecting the isotopic mass fraction of heavier isotopes⁶. Moreover, the photospheric abundances observed today are different from those existing at the beginning of the solar system (4.6 Gyr ago), because of the element settling from the solar photosphere into the Sun’s interior. Lodders, Palme & Gail (2009) found that original protosolar values of elements heavier than He (Z) were $\sim 13\%$ larger than observed today (whereas He increases by about $\sim 15\%$).

In Fig. 3, we show updated GCE results normalized to solar abundances by Lodders, Palme & Gail 2009 (*black symbols*) and Anders & Grevesse (1989) (*grey symbols*; as made by Travaglio et al. 2004). Noteworthy solar abundance variations⁷ ($>10\%$) are CNO ($\sim -30\%$), P ($\sim -20\%$), S (-25%), Cl ($+37\%$), Kr ($+24\%$), Nb ($+13\%$), I ($+22\%$), Xe ($+16\%$), and Hg ($+35\%$).

Additional differences between the GCE results shown in Table 1 derive from experimental cross section measurements and theoretical nuclear improvements provided in the last decade.

New GCE calculations include the recent theoretical evaluation of the $^{22}\text{Ne}(\alpha, n)^{25}\text{Mg}$ rate by Longland, Iliadis & Karakas (2012), which is based on the direct experimental measurement by Jaeger et al. (2001). At AGB temperatures ($T_8 \sim 2.5$ to 3.5) the $^{22}\text{Ne}(\alpha, n)^{25}\text{Mg}$ rate by Longland, Iliadis & Karakas (2012) is very close to the value by Jaeger et al. (2001), and it is about a factor of two lower than the rate we used so far: the lowest

⁶Note that about half of solar Z abundances (where Z is the sum of all elements heavier than helium, called "metals" in stars) comes from oxygen, followed by carbon, neon, nitrogen (silicon, magnesium and iron as well).

⁷Variations refer to values normalized to the number of silicon atoms $N(\text{Si}) = 10^6$.

limit by Käppeler et al. (1994)⁸. The $^{22}\text{Ne}(\alpha, n)^{25}\text{Mg}$ neutron source produces variations of the s -isotopes close to the branching points: updated GCE calculations have reduced the s -contribution to few light isotopes, ^{86}Kr , $^{85,87}\text{Rb}$, ^{96}Zr (and the s -only ^{96}Mo), with a complementary increase of $^{86,87}\text{Sr}$, owing to the branches at ^{85}Kr , ^{86}Rb and ^{95}Zr . Minor effects ($<10\%$) are seen for heavier isotopes (see Bisterzo et al. 2013, Fig. 1, bottom panel). A discussion of the major branching points of the s -process and the effect of the new $^{22}\text{Ne}(\alpha, n)^{25}\text{Mg}$ rate will be given in Bisterzo et al., in preparation.

Particularly large was the total s -production of ^{96}Zr obtained in 2004 ($\sim 80\%$). Updated GCE results predict that about half of solar ^{96}Zr comes from AGB stars ($\sim 3\%$ from IMS and $\sim 36\%$ from LMS; see Table 1). Travaglio et al. (2011) estimated an additional non-negligible p -process contribution to ^{96}Zr by SNeIa (up to 30%).

However, we remind that ^{96}Zr is strongly sensitive to the $^{95}\text{Zr}(n, \gamma)^{96}\text{Zr}$ rate, which is largely uncertain being evaluated only theoretically. In this regard, we adopt a rate roughly half the value recommended by Bao et al. (2000), close to that by Toukan & Käppeler (1990), in agreement with Zr isotopic measurements in presolar SiC grains (Lugaro et al. 2003). Recently, Lugaro et al. (2014) provide a lower estimation of the $^{95}\text{Zr}(n, \gamma)^{96}\text{Zr}$ rate: at $kT \sim 23$ keV, their value is roughly three times lower than that by Bao et al. (2000) and about half of that by Toukan & Käppeler (1990). This results in a decreased GCE s -contribution to solar ^{96}Zr by $\sim 10\%$.

Moreover, ^{96}Zr depends on the number of TPs experienced by the adopted AGB models. Our LMS models with $M = 1.5, 2$ and $3 M_{\odot}$ experience several TPs with TDU, from 20 to

⁸The lowest limit by Käppeler et al. (1994) has been evaluated by neglecting the resonance contribution at 633 keV. Note that, at AGB temperatures, the $^{22}\text{Ne}(\alpha, \gamma)^{26}\text{Mg}$ rates recommended by Jaeger et al. (2001) and Longland, Iliadis & Karakas (2012) are in agreement with the lower limit evaluated by Käppeler et al. (1994).

35 TPs depending on the mass and metallicity (Bisterzo et al. 2010, their Table 2), reaching temperatures high enough to partly activate the $^{22}\text{Ne}(\alpha, n)^{25}\text{Mg}$ neutron source and to open the branch at ^{96}Zr . A stronger mass loss would partly reduce the s contribution to ^{96}Zr from LMS AGB stars.

On the other side, our $M = 5$ and $7 M_{\odot}$ models experience 24 TPs. Given the large uncertainty affecting the treatment of mass loss in IMS (Section 2.2), the number of TPs may increase by a factor of three or more (in particular for $M = 7 M_{\odot}$ models), leading to a greater overall amount of material dredged up. Owing to the dominant s -contribution from LMS stars over IMS, the general effect on solar GCE prediction would be negligible even by increasing the mass of the TDU in both $M = 5$ and $7 M_{\odot}$ models several times. Exceptions are ^{86}Kr , ^{87}Rb , and ^{96}Zr , which receive a non-negligible contribution from IMS stars: by increasing the TDU mass of IMS by a factor of six, the solar prediction to ^{96}Zr increases from $\sim 40\%$ up to $\sim 60\%$; similar variations affect ^{86}Kr ($\sim +20\%$), larger effects are shown by ^{87}Rb (from $\sim 30\%$ up to $\sim 70\%$).

As discussed in Section 2.2, new IMS yields are computed with a negligible ^{13}C -pocket; instead, Travaglio et al. (2004) assumed that a ^{13}C -pocket with $M(^{13}\text{C}) = 10^{-7} M_{\odot}$ could form in IMS, yielding an increase of $\sim 10\%$ to solar ^{96}Zr , $\sim 3\%$ to ^{86}Kr and $\sim 6\%$ to ^{87}Rb . Solar GCE predictions of isotopes with $A > 100$ show marginal variations, because the ^{13}C -pocket contribution from IMS is almost negligible (up to a few percent) when compared to that of LMS.

New neutron capture cross section measurements further modify the s -process distribution. Travaglio et al. (2004) adopted the compilation by Bao et al. (2000), while we refer to KADoNiS (as well as few additional measurements listed above). Important variations come from the new $^{139}\text{La}(n, \gamma)^{140}\text{La}$ rate by Winckler et al. (2006), the $^{180}\text{Ta}^m(n, \gamma)^{181}\text{Ta}$ rate by Wisshak et al. (2004) (including the revised stellar enhancement factor, SEF, by KADoNiS), and the improved treatment of the branch at ^{176}Lu , which modifies

the $^{176}\text{Lu}/^{176}\text{Hf}$ ratio (Heil et al. 2008). The solar s -contribution to La, often used as a reference element to disentangle between s and r process enrichment in the atmosphere of peculiar stars, increases by $\sim+10\%$ (from 63% to 76%, see Table 1). The solar s -production of $^{180}\text{Ta}^m$ increases from $\sim 50\%$ to $\sim 80\%$, substantially reducing the contribution expected from the p -process.

Discrepancies of $\sim 10\%$ for ^{154}Gd and ^{160}Dy , and $\sim 20\%$ for ^{192}Pt (see Section 2.4) suggest that large uncertainties affect the neutron capture cross sections at stellar energy (e.g., SEF evaluation) for isotopes with $A > 150$. Note that ^{160}Dy may receive a small contribution from p -process (Travaglio et al. 2011). Despite all Pb isotopes have well determined neutron capture cross sections (see KADoNiS), the contribution to the s -only ^{204}Pb is affected by the branch at ^{204}Tl , which produces variations of $\sim 10\%$.

Finally, as recalled above, the new GCE predictions adopt an extended range of AGB yields, including $M = 1.3, 1.4$ and $2 M_{\odot}$ models. In Travaglio et al. (2004), only $M = 1.5$ and $3 M_{\odot}$ models among LMS were used for GCE calculations. AGB stars with initial mass of $M = 1.3$ and $1.4 M_{\odot}$ experience five and ten TPs followed by TDU, respectively (Bisterzo et al. 2010). This results in an additional s -process contribution of about 5% and 10% at the epoch of the solar system, without modifying the s -distribution. Note that for metallicities higher than $[\text{Fe}/\text{H}] \sim -0.6$, $M = 1.3 M_{\odot}$ models do not contribute to the chemical evolution of the Galaxy because the conditions for the activation of the TDU episodes are never reached in our models (see Straniero et al. 2003). The addition of $M = 2 M_{\odot}$ yields in GCE computations provides an increase of about 10% of the predicted solar ^{208}Pb , and smaller variations to isotopes with $A \lesssim 140$ (lower than 5%), with the exception of solar ^{96}Zr (which is 10% lower). AGB stars with $M = 1.5$ and $2 M_{\odot}$ predict comparable s -process abundances because both models reach similar temperatures during convective TPs and the larger overall amount of material dredged up

by the $2 M_{\odot}$ model (which experiences about six more TDUs than the $1.5 M_{\odot}$ model) is diluted with a more extended envelope (Bisterzo et al. 2010). Thus, in both 1.5 and $2 M_{\odot}$ models the marginal activation of the $^{22}\text{Ne}(\alpha, n)^{25}\text{Mg}$ produces a smaller s -process contribution to the first s -peak (including ^{96}Zr) than in $3 M_{\odot}$ models, while on average ^{208}Pb is favored, being the $^{13}\text{C}(\alpha, n)^{16}\text{O}$ reaction the main source of neutrons. Instead, AGB stars with initial mass of $M = 3 M_{\odot}$ and $[\text{Fe}/\text{H}] \sim -1$ reach higher temperatures at the bottom of the TPs ($T_8 = 3.5$), feeding more efficiently the first and second s -peaks than ^{208}Pb . As consequence, linear interpolations between $M = 1.5$ and $3 M_{\odot}$ yields, as previously made by Travaglio et al. (2004), induced up to 10% differences in ^{96}Zr and ^{208}Pb solar predictions.

Updated GCE calculations plausibly interpret within the nuclear and solar uncertainties all s -only isotopes with $A > 130$.

The understanding of the origin of light s -process isotopes with $A \leq 130$ remains enigmatic: we confirm the missing $\sim 25\%$ predicted solar s -contribution to isotopes from ^{86}Sr to ^{130}Xe (including the s -only ^{96}Mo , ^{100}Ru , ^{104}Pd , ^{110}Cd , ^{116}Sn , $^{122,123,124}\text{Te}$ and $^{128,130}\text{Xe}$) firstly found by Travaglio et al. (2004). Few of them may receive an additional small contribution from the p -process (e.g., 2% to ^{96}Mo , 5% to ^{110}Cd , 3% to ^{122}Te and 6% to ^{128}Xe ; Travaglio et al. 2011).

In Section 3, we explore the effect of the ^{13}C -pocket uncertainty in LMS on GCE predictions at the epoch of the solar-system formation.

2.4. New neutron capture rates for Pt and ^{192}Ir isotopes

The solar s -only ^{192}Pt predicted by GCE model is about 20% lower than measured in the solar system. So far, we considered this value plausible within the known uncertainties:

the KADoNiS recommended $^{192}\text{Pt}(n, \gamma)^{193}\text{Pt}$ rate has 20% of uncertainty (590 ± 120 mbarn at 30 keV; Bao et al. 2000), the neutron capture cross sections of ^{191}Os and ^{192}Ir are evaluated theoretically at 22%, and the solar Pt abundance is known with 8% of uncertainty (Lodders, Palme & Gail 2009).

Recently, Koehler & Guber (2013) measured the neutron capture cross sections of Pt isotopes with much improved accuracy, and used their experimental results to provide a new theoretical estimation of the $^{192}\text{Ir}(n, \gamma)$ rate. The new Maxwellian-Averaged Cross Sections (MACS) of $^{192}\text{Pt}(n, \gamma)^{193}\text{Pt}$ (483 ± 20 mbarn at 30 keV; 4% uncertainty) is $\sim 20\%$ lower than that recommended by KADoNiS, suggesting an increased ^{192}Pt prediction ($\sim 90\%$), in better agreement with the solar value. On the other side, the theoretical $^{192}\text{Ir}(n, \gamma)$ rate estimated by Koehler & Guber (2013) is much larger (about $+50\%$) than that by KADoNiS (2080 ± 450 mbarn at 30 keV), reducing again the s -contribution to ^{192}Pt .

The new GCE prediction of solar ^{192}Pt obtained by including neutron capture rates of Pt isotopes and ^{192}Ir by Koehler & Guber (2013) is $\sim 78\%$. This value may increase up to $\sim 85\%$ by considering the uncertainty of the theoretical $^{192}\text{Ir}(n, \gamma)$ rate ($\pm 22\%$), and up to 93% by adopting a 2σ uncertainty.

More detailed analyses on ^{192}Ir MACS would help to improve the understanding of this branching point and to provide a more accurate solar ^{192}Pt estimation (e.g., Rauscher 2012).

3. Effect of the ^{13}C -pocket uncertainty in LMS on GCE predictions at the epoch of the solar-system formation

As discussed in Section 1, the problem of the formation of the ^{13}C -pocket is still unsolved. The tests on the ^{13}C -pocket discussed in this work allow us to explore the impact of different shapes and sizes of the adopted ^{13}C -pocket on the s -process yields.

The internal structure of the ^{13}C -pocket adopted so far is specified in Table 2 (first group of data): it is a three-zone ^{13}C -pocket (zones I-II-III roughly correspond to those described by Gallino et al. 1998, their Fig. 1), each one has defined $X(^{13}\text{C})$ and $X(^{14}\text{N})$ abundances, and a total ^{13}C mass of $\sim 5 \times 10^{-6} M_{\odot}$ ($\sim 2 \times 10^{-7} M_{\odot}$ of ^{14}N). The total mass of the three-zone pocket is about the twentieth part of a typical convective TP in LMS ($M(\text{pocket}) \sim 0.001 M_{\odot}$). This corresponds to the so-called case ST. As anticipated in Section 2.2, case ST is calibrated to reproduce the solar *main* component (Arlandini et al. 1999).

Note that case ST differs from a H profile that exponentially decreases starting from the envelope value $X(\text{H}) = 0.7$. In such a case an outer ^{14}N -rich zone, also called ^{14}N -pocket, forms in the outer layers of the He-intershell (Goriely & Mowlavi 2000; Cristallo et al. 2009; Karakas et al. 2010; Lugaro et al. 2012).

To evaluate the impact of different ^{13}C -pocket structures on GCE predictions at the solar epoch, we made a few tests in which we introduced different $X(^{13}\text{C})$ profiles and total masses in the pocket, both considered as free parameters in LMS. We remind that the effect of the ^{13}C -pocket in IMS is negligible for GCE predictions at $t_{\odot} = 9.2$ Gyr (see Section 2). Starting from the three-zone ^{13}C profile used so far, we exclude the two external ^{13}C -rich zones of the pocket (leaving zone II only) in order to obtain flat ^{13}C and ^{14}N profiles. We still adopt a range of ^{13}C -pocket strengths by multiplying the abundances of ^{13}C and ^{14}N from 0.1 to 2 times the values of zone II.

In addition, we test the effects of the variation of the mass of the pocket $M(\text{pocket})$, both on the three-zone ^{13}C -pocket and zone-II ^{13}C -pocket.

The internal structure of the ^{13}C -pocket adopted in the different tests is specified in Table 2.

As a first test, we increase the mass of the pocket by a factor of two, keeping unchanged the amount of ^{13}C and ^{14}N in the three zones of the ^{13}C -pocket (see Fig. 4, *filled triangles*).

For comparison we also represent with *filled circles* the s -process distribution shown in Fig. 2. Intuitively, if we adopt the same weighted average of the various ^{13}C -pocket strengths as performed before, one should obtain an overestimation by a factor of two of the whole s -process abundance distribution. Effectively, we predict 200% of solar ^{136}Ba , 230% of solar ^{150}Sm and 300% of solar ^{208}Pb . We already recalled that, in order to reconcile GCE predictions with solar abundances, we have the freedom to change the weighted average among the various ^{13}C -pocket strengths: specifically, we exclude case $\text{ST}\times 1.3$ from the ^{13}C -pocket average and we reduce the weight of case ST to 20% (see Fig. 5, *filled triangles*). This may be justified in the framework of the observed s -process spread, which, within the large degree of current AGB model uncertainties, we compute with a range of ^{13}C -pocket strengths.

As a second test, we reduce the mass of the three-zone ^{13}C -pocket by a factor of two (see Fig. 4, *filled down-rotated-triangles*). The predicted solar s -contributions are reduced to 48% of solar ^{136}Ba , 43% of solar ^{150}Sm and 37% of solar ^{208}Pb . As shown in Fig. 5 (*filled down-rotated-triangles*), this underestimation can be solved by fully including case $\text{ST}\times 1.3$ (which in our standard GCE calculation is considered at $\sim 25\%$, Section 2.3) in the ^{13}C -pocket average.

As consequence, an increased or decreased mass of the ^{13}C -pocket by a factor of two in all LMS models marginally affects the predicted solar s -process distribution obtained with a weighted average of ^{13}C -pocket strengths.

Similar solutions are achieved by the two additional tests computed with flat ^{13}C profiles (see Fig. 5): zone-II ^{13}C -pockets with $M(\text{pocket}) \sim 0.0005 M_{\odot}$ (*empty circles*), and $M(\text{pocket}) \sim 0.001 M_{\odot}$ (*empty squares*), which corresponds to the mass of zone II of our standard pocket multiplied by a factor of two. By giving different weights to cases $\text{ST}\times 1.3$ and ST, which dominate the average of ^{13}C -pocket strengths, the solar s -distribution

predicted by GCE model shows variations within the solar uncertainties: $\lesssim 5\%$ for s -only isotopes from $A = 140$ to 210 and $A = 100$ to 125 , and up to $\sim 5\%$ for $^{134,136}\text{Ba}$ and $^{128,130}\text{Xe}$. More evident variations ($\gtrsim 10\%$) are displayed by few isotopes lighter than $A = 100$, e.g., $^{86,87}\text{Sr}$ and ^{96}Zr , which, however, receive an additional contribution by other astrophysical sources (e.g., weak- s process, p -process).

The deficit of the predicted solar s -abundances for isotopes from $A = 90$ to 130 remains unchanged with the tests shown in Fig. 5.

In summary, according to an s -distribution referred to ^{150}Sm , the need of an additional s -process between $A = 90$ and 130 (LEPP- s , given that s -only isotopes also show the missing contribution) is confirmed by updated GCE results. Specifically, the need of LEPP- s is independent of the most significant ^{13}C -pocket tests we carried out in this paper. This result supports the presence of an s -process in massive stars during the pre-explosive phases that follow the core He-burning and convective shell C-burning phases. According to Pignatari et al. (2010), the *weak-s* process may produce Sr-Y-Zr in larger amount (up to $\sim 30\%$) than previously estimated by Raiteri, Gallino, & Busso (1992) ($< 10\%$). However, while the *weak-s* contribution estimated for lighter trans-iron elements (e.g., Cu) is plausibly established because they are weakly affected by uncertainties of nuclear rates, C shell evolution, neutron density history, or initial composition, heavier isotopes as Sr show larger sensitivity to stellar models and nuclear uncertainties. Recent investigations suggest that the s -contribution from massive stars may extend to heavier elements, with a bulk of the production at Sr-Y-Zr and, in minor amount, up to Te-Xe (Pignatari et al. 2013).

4. Conclusions

We study the solar abundances of heavy s -isotopes at the epoch of the formation of the solar system as the outcome of nucleosynthesis occurring in AGB stars of various masses and metallicities. At present, one of the major uncertainties of AGB stellar model is the formation of the ^{13}C -pocket. Our aim is to investigate the impact of uncertainties concerning the internal structure of the ^{13}C -pocket on the GCE s -distribution, by carrying out different tests in which we modify the ^{13}C and ^{14}N abundances in the pocket, and the size in mass of the pocket itself. Thereby, we obtain that GCE s -process predictions at the epoch of the solar-system formation marginally depend on the choice of the ^{13}C profile and on the mass of the pocket when a range of ^{13}C -pocket strengths is adopted. The GCE model may reproduce within the solar error bars the s -contribution to isotopes with $A > 130$. The missing contribution to isotopes in the range between $A = 90$ to 130 found by Travaglio et al. (2004) is confirmed by the present analysis: an additional s -process (LEPP- s) is required to account for the missing component of ten s -only isotopes (^{96}Mo , ^{100}Ru , ^{104}Pd , ^{110}Cd , ^{116}Sn , $^{122,123,124}\text{Te}$ and $^{128,130}\text{Xe}$). Based on the tests made in this paper, the LEPP- s contribution remains essentially the same, independently of the internal structure of the ^{13}C -pocket. First indications in favor of this process have been analyzed and discussed by Pignatari et al. (2013).

An additional primary contribution is being explored to account for a complementary light- r contributions. In spite of promising theoretical improvements related to the explosive phases of massive stars and core collapse Supernovae (Arcones & Thielemann 2013 and references therein), as well as recent spectroscopic investigations (Roederer 2012; Hansen et al. 2012, 2013), a full understanding of the origin of the neutron capture elements from Sr up to Xe is still lacking.

We are extremely indebted with the anonymous referee for helpful comments, which

have significantly improved the structure and clarity of the paper. S.B. was supported by a JINA Fellowship (ND Fund #201387 and 305387). Numerical calculations have been sustained by B2FH Association (<http://www.b2fh.org/>).

REFERENCES

- Abia, C., Busso, M., Gallino, R., Domínguez, I., Straniero, O., & Isern, J. 2001, *ApJ*, 1117, 1134
- Abia, C., Domínguez, I., Gallino, R. et al. 2002, *ApJ*, 579, 817
- Allen, D., & Barbuy, B. 2006, *A&A*, 454, 917
- Anders, E., & Grevesse, N. 1989, *Geochim. Cosmochim. Acta*, 53, 197
- Aoki, W., Ryan, S. G., Norris, j. E., Beers, T. C., Ando, H., & Tsangarides, S. 2002, *ApJ*, 580, 1149
- Arcones, A., & Thielemann, F.-K. 2013, *Journal of Physics G: Nuclear and Particle Physics*, 40, 013201
- Arlandini, C., Käppeler, F., Wisshak, K., Gallino, R., Lugaro, M., Busso, M., & Straniero, O. 1999, *ApJ*, 525, 886
- Asplund, M. 2005, *ARA&A*, 43, 481
- Bao, Z. Y., Beer, H., Käppeler F., Voss, F., & Wisshak, K. 2000, *Atomic Data & Nuclear Data Tables*, 76, 70
- Bennett, C. L., Larson, D., Weiland, J. L. et al. 2013, *ApJS*, 208, 20
- Best, J., Stoll, H., Arlandini, C., et al. 2001, *Phys. Rev. C*, 64, 015801
- Bisterzo, S., Travaglio, C., Wiescher, M., Gallino, R. et al. 2013, *Journal of Physics: Conference Series (JPCS)*, Nuclear Physics in Astrophysics VI (NPA-VI), Lisbon, Portugal, May 19th–24th, in press (ArXiv e-prints, arXiv:1311.5381)

- Bisterzo, S., Gallino, R., Straniero, O., Cristallo, S., & Käppeler, F. 2011, MNRAS, 418, 284
- Bisterzo, S., Gallino, R., Straniero, O., Cristallo, S., & Käppeler, F. 2010, MNRAS, 404, 1529
- Boothroyd, A. I., & Sackmann, I.-J. 1988, ApJ, 328, 653
- Burbidge, E. M., Burbidge, G. R., Fowler, W. A., & Hoyle, F. 1957, Rev. Mod. Phys., 29, 547
- Busso, M., Palmerini, S., Maiorca, E., Trippella, O., Magrini, L., & Randich, S. 2012, 12th Symposium on Nuclei in the Cosmos, August 5 - 12, Cairns, Australia, 20
- Busso, M., Wasserburg, G. J., Nollett, K. M., & Calandra, A. 2007, ApJ, 671 802
- Busso, M., Gallino, R., Lambert, D. L., Travaglio, C., & Smith, V. V. 2001, ApJ, 557, 802
- Cameron, A. G. W. 1957, AJ, 62, 9
- Clayton, D. D., & Rassbach, M. E. 1967, ApJ, 168, 69
- Clayton, D. D., & Nittler, L. R. 2004, ARA&A, 42, 39
- Cristallo, S., Piersanti, L., Straniero, O., Gallino, R., Domínguez, I., Abia, C., Di Rico, G., Quintini, M., & Bisterzo, S. 2011, ApJS, 197, 17
- Cristallo, S., Straniero, O., Gallino, R., Piersanti, L., Domínguez, I., & Lederer, M. T. 2009, ApJ, 696, 797
- Denissenkov, P. A., & Tout, C. A. 2003, MNRAS, 340, 722
- Doherty, C. L., Gil-Pons, P., Lau, H. H. B., Lattanzio, J. C., & Siess, L. 2014, MNRAS, 437, 195

- Domínguez, I., Chieffi, A., Limongi, M., & Straniero, O. 1999, *ApJ*, 524, 226
- D’Orazi, V.; Lugaro, M., Campbell, S. W., Bragaglia, A., Carretta, E., Gratton, R. G.,
Lucatello, S., & D’Antona, F. 2013, *ApJ*, 776, 59
- Frischknecht, U., Hirschi, R., & Thielemann, F.-K. 2012, *A&A*, 538, L2
- Gallino, R., Arlandini, C., Busso, M., Lugaro, M., Travaglio, C., Straniero, O., Chieffi, A.,
& Limongi, M. 1998, *ApJ*, 497, 388
- García-Hernández, D. A., Zamora, O., Yagüe, A., Uttenthaler, S., Karakas, A. I., Lugaro,
M., Ventura, P., & Lambert, D. L. 2013, *A&A*, 555, L3
- García-Hernández, D. A., Manchado, A., Lambert, D. L., Plez, B., García-Lario, P.,
D’Antona, F., Lugaro, M., Karakas, A. I., & van Raai, M. A. 2009, *ApJ*, 705, 31
- Goriely, S., & Siess, L. 2004, *A&A*, 421, L25
- Goriely, S., & Mowlavi, N. 2000, *A&A*, 362, 599
- Hansen, C. J., Primas, F., Hartman, H., et al. 2012, *A&A*, 545, 31
- Hansen, C. J., Bergemann, M., Cescutti, G., François, P., Arcones, A., Karakas, A. I., Lind,
K., & Chiappini, C. 2013, *A&A*, 551, A57
- Hayakawa, T., Iwamoto, M., Kajino, T., Shizuma, T., Umeda, H., & Nomoto, K. 2008,
ApJ, 685, 1089
- M. Heil, M., Juseviciute, A., Käppeler, F., Gallino, R., & Pignatari, M., Uberseder, E.,
2009, *PASA*, 26, 243
- Heil, M., Winckler, N., Dababneh, S., et al. 2008, *ApJ*, 673, 434
- Herwig, F. 2005, *ARA&A*, 43, 435

- Herwig, F. 2004, *ApJ*, 605, 425
- Herwig F. Langer N., & Lugaro M., 2003, *ApJ*, 593, 1056
- Herwig, F., Blöcker, T., Schönberner, D., & El Eid, M. 1997, *A&A*, 324, L81
- Howard, W. M., Meyer, B. S., & Woosley, S. E. 1991, *ApJ*, 373, 5
- Iben, I. Jr, & Renzini, A. 1983, *ARA&A*, 21, 271
- Israelian, G., Rebolo, R., García López, R. J., Bonifacio, P., Molaro, P., Basri, G., & Shchukina, N. 2001, *ApJ*, 551, 833
- Jaeger, M., Kunz, R., Mayer, A., Hammer, J. W., Staudt, G., Kratz, K. L., & Pfeiffer, B. 2001, *Phys. Rev. Lett.*, 87, 202501
- Jonsell, K., Barklem, P. S., Gustafsson, B., Christlieb, N., Hill, V., Beers, T. C., Holmberg, J. 2006, *A&A*, 451, 651
- Käppeler, F., Gallino, R., Bisterzo, S., & Aoki, W. 2011, *Rev. Mod. Phys.*, 83, 157
- Käppeler, F., Wiescher, M., Giesen, U., et al. 1994, *ApJ*, 437, 396
- Karakas, A. I., García-Hernández, D. A., & Lugaro, M. 2012, *ApJ*, 751, 8
- Karakas, A. I. 2010, *MNRAS*, 403, 1413
- Karakas, A., & Lattanzio, J. 2003, *PASA*, 20, 279
- Koehler, P. E., & Guber, K. H. 2013, *Phys. Rev. C.*, 88, 035802
- Lai, D. K., Bolte, M., Johnson, J. A., Lucatello, S., Heger, A., & Woosley, S. E. 2008, *ApJ*, 681, 1524
- Lambert, D. L., Smith, V. V., Busso, M., Gallino, R., & Straniero, O. 1995, *ApJ*, 450, 302

- Langer, N., Heger, A. Wellstein, S., & Herwig, F. 1999, *A&A*, 346, L37
- Lau, H. H. B., Stancliffe, R. J., & Tout, C. A. 2009, *MNRAS*, 396, 1046
- Lederer, C., Massimi, C., Altstadt, S., et al. 2013, *Phys. Rev. Lett.*, 110, 022501
- Lodders, K., Palme, H., & Gail, H.-P. 2009, *Landolt-Börnstein - Group VI Astronomy and Astrophysics Numerical Data and Functional Relationships in Science and Technology*, Edited by J.E. Trümper, 4B: solar system, 4.4
- Longland, R., Iliadis, C., & Karakas, A. I. 2012, *Phys. Rev. C*, 85, 065809
- Lugaro, M., Tagliente, G., Karakas, A. I., Milazzo, P. M., Käppeler, F., Davis, A. M., & Savina, M. R. 2014, *ApJ*, 780, 95
- Lugaro, M., Karakas, A., Stancliffe, R. J., & Rijs, C. 2012, *ApJ*, 747, 2
- Lugaro, M., Davis, A. M., Gallino, R., Pellin, M. J., Straniero, O. & Käppeler, F. 2003, *ApJ*, 593, 486
- Marganiec, J., Dillmann, I., Domingo Pardo, C., Käppeler, F., & Walter, S., 2010, *Phys. Rev. C*, 82, 035806
- Massimi, C., Koehler, P., Bisterzo, S., et al. 2012, *Phys. Rev. C*, 85, 044615
- Meléndez, J., Shchukina, N. G., Vasiljeva, I. E., & Ramírez, I. 2006, *ApJ*, 642, 1082
- Mishenina, T. V., Pignatari, M., Korotin, S. A., Soubiran, C., Charbonnel, C., Thielemann, F.-K., Gorbaneva, T. I., & Basak, N. Yu. 2013, *A&A*, 552, 128
- Mosconi, M., Fujii, K., Mengoni, A., et al. 2010, *Phys. Rev. C*, 82, 015802
- Mutti, P., Beer, H., Brusegan, A., Corvi, F., & Gallino, R. 2005, *AIP Conf. Proc.*, 769, 1327, INTERNATIONAL CONFERENCE ON NUCLEAR DATA FOR SCIENCE

AND TECHNOLOGY, 26 September – 1 October 2004, Santa Fe, New Mexico
(USA)

Nissen, P. E., Primas, F. Asplund, M. & Lambert, D. L. 2002, *A&A*, 390, 235

Palme, H., & Beer, H. 1993, in Landolt Börnstein Group VI, *Astronomy and Astrophysics*,
Vol. 2A, ed. H. H. Voigt (Berlin: Springer), 196

Patronis, N., Dababneh, S., Assimakopoulos, P. A., et al. 2004, *Phys. Rev. C*, 69, 025803

Péquignot, D., & Baluteau, J.-P. 1994, *A&A*, 283, 593

Piersanti, L., Cristallo, S., & Straniero, O. 2013, *ApJ*, arXiv:1307.2017

Pignatari, M., Hirschi, R., Wiescher, M. et al. 2013, *ApJ*, 762, 31

Pignatari, M., Gallino, R., Heil, M., Wiescher, M., Käppeler, F., Herwig, F., & Bisterzo, S.
2010, *ApJ*, 710, 1557

Raiteri, C. M., Gallino, R., & Busso, M. 1992, *ApJ*, 387, 263

Ramírez, I., Allende Prieto, C., & Lambert, D. L. 2013, *ApJ*, 764, 78

Ramírez, I., Meléndez, J., & Chanamé, J. 2012, *ApJ*, 757, 164

Rauscher, T. 2012, *ApJ*, 755, 10

Rauscher, T., Heger, A., Hoffman, R. D., & Woosley, S. E. 2002, *ApJ*, 576, 323

Reifarth, R., Dababneh, S., Heil, M., Käppeler, F., Plag, R., Sonnabend, K., & Uberseder,
E. 2012, *Phys. Rev. C*, 85, 035802

Reifarth, R., Arlandini, C., Heil, M., et al. 2003, *ApJ*, 582, 1251

Reifarth, R., Heil, M., Käppeler, et al. 2002, *Phys. Rev. C*, 66, 064603

- Reyniers, M., Abia, C., Van Winckel, H., Lloyd Evans, T., Decin, L., Eriksson, K., & Pollard, K. 2007, *A&A*, 461, 641
- Roederer, I. U. 2012, *ApJ*, 756, 36
- Seeger, P. A., Fowler, W. A., & Clayton, D. D. 1965, *ApJS*, 11, 121
- Serminato, A., Gallino, R., Travaglio, C., Bisterzo, S., & Straniero, O. 2009 *PASA*, 26, 153
- Sharpee, B., Zhang, Y., Williams, R., Pellegrini, E., Cavagnolo, K., Baldwin, J. A., Phillips, M., & Liu, X.-W. 2007, *ApJ*, 659, 1265
- Spite, M., Cayrel, R., Plez, B., et al. 2005, *A&A*, 430, 655
- Sterling, N. C., & Dinerstein, H. L. 2008, *ApJS*, 174, 158
- Siess, L. 2010, *A&A*, 512, A10
- Siess, L., Goriely, S., & Langer, N. 2004, *A&A*, 415, 1089
- Smith, V. V., & Lambert, D. L. 1990, *ApJS*, 72, 387
- Snedden, C., Cowan, J. J., & Gallino, R. 2008, *ARA&A*, 46, 241
- Snedden, C., Cowan, J. J., Lawler, J. E. et al. 2003, *ApJ*, 591, 936
- Spergel, D. N., Verde, L., Peiris, H. V. et al. 2003, *ApJS*, 148, 175
- Straniero, O., Gallino, R., & Cristallo, S. 2006, *Nucl. Phys. A*, 777, 311
- Straniero, O., Domínguez, I., Cristallo, S., & Gallino, R. 2003, *PASA*, 20, 389
- Straniero, O., Limongi, M., Chieffi, A., Domínguez, I., Busso, M., & Gallino, R. 2000, *Mem. Soc. Astron. Ital.*, 71, 719

- Straniero, O., Gallino, R., Busso, M., Chieffi, A., Raiteri, C. M., Limongi, M., Salaris, M. 1995, *ApJ*, 440, L85
- Tagliente, G., Milazzo, P. M., Fujii, K., et al. 2011, *Phys. Rev. C*, 84, 015801
- Tagliente, G., Milazzo, P. M., Fujii, K., et al. 2011a, *Phys. Rev. C*, 84, 055802
- Tagliente, G., Milazzo, P. M., Fujii, K., et al. 2010, *Phys. Rev. C*, 81, 055801
- Thielemann, F.-K., Arcones, A., Käppeli, R. et al. 2011, *Progress in Particle and Nuclear Physics*, 66, 346
- Tomkin, J., & Lambert, D. L. 1999, *ApJ*, 523, 234
- Toukan, K., & Käppeler, F. 1990, *ApJ*, 348, 357
- Travaglio, C., Röpke, F. K., Gallino, R., & Hillebrandt, W., 2011, *ApJ*, 739, 93
- Travaglio, C., Gallino, R., Arnone, E., Cowan, J., Jordan, F., & Sneden, C. 2004, *ApJ*, 601, 864
- Travaglio, C., Hillebrandt, W., Reinecke, M., & Thielemann, F.-K. 2004a, *A&A*, 425, 1029
- Travaglio, C., Gallino, R., Busso, M., & Gratton, R. 2001, *ApJ*, 549, 346
- Travaglio, C., Galli, D., Gallino, R., Busso, M., Ferrini, F., & Straniero, O. 1999, *ApJ*, 521, 691
- Van Eck, S. Goriely, S., Jorissen, A., & Plez, B. 2001, *Nature*, 412, 793
- van Raai, M. A., Lugaro, M., Karakas, A. I., García-Hernández, D. A., & Yong, D. 2012, *A&A*, 540, 44
- Ventura, P., Di Criscienzo, M., Carini, R., & D’Antona, F. 2013, *MNRAS*, 431, 3642

Ventura, P., & D'Antona, F. 2005, *A&A*, 431, 279

Ventura, P., & D'Antona, F. 2005a, *A&A*, 439, 1075

Winckler, N., Dababneh, S., Heil, M. et al. 2006, *ApJ*, 647, 685

Wisshak, K., Voss, F., Arlandini, C., Käppeler, F., Heil, M., Reifarth, R., Krticka, M., & Becvar, F. 2004, *Phys. Rev. C*, 69, 055801

Yong, D., Lambert, D. L., Paulson, D. B., & Carney, B. W. 2008, *ApJ*, 673, 854

Zamora, O., Abia, C., Plez, B., Domnguez, I., & Cristallo, S. 2009, *A&A*, 508, 909

Zinner, E. 2007, *Presolar grains. Meteorites, Planets, and Comets, Treatise on Geochemistry*, eds A.M. Davis, H.D. Holland, and K.K. Turekian (Elsevier, Oxford), published electronically at <http://www.sciencedirect.com/science/referenceworks/9780080437514>, 2nd Ed, Vol. 1.

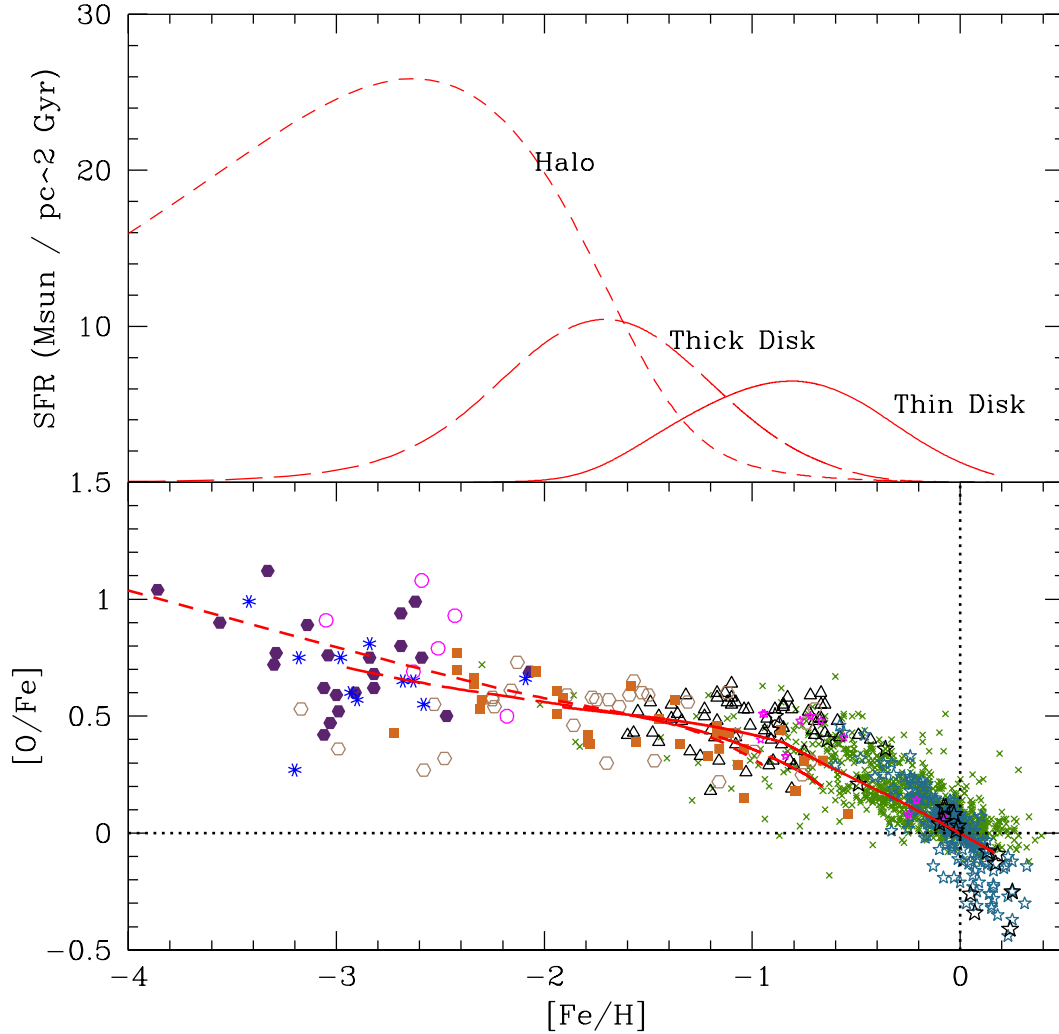


Fig. 1.— Star formation rate (*top panel*) and $[\text{O}/\text{Fe}]$ (*bottom panel*) obtained with GCE models as a function of $[\text{Fe}/\text{H}]$. $[\text{O}/\text{Fe}]$ predictions are compared with spectroscopic observations by Spite et al. (2005) (filled hexagons), Lai et al. (2008) (asterisks), Israelian et al. (2001) (empty circles), Meléndez et al. (2006) (empty hexagons), Nissen et al. (2002) (filled squares), Ramírez, Allende Prieto, & Lambert (2013) (crosses), Ramírez, Meléndez, & Chanamé (2012) (empty triangles), Mishenina et al. (2013) (small, middle and big stars for thick, thin, and unclassified stars, respectively). *See the electronic paper for a color version of this Figure.*

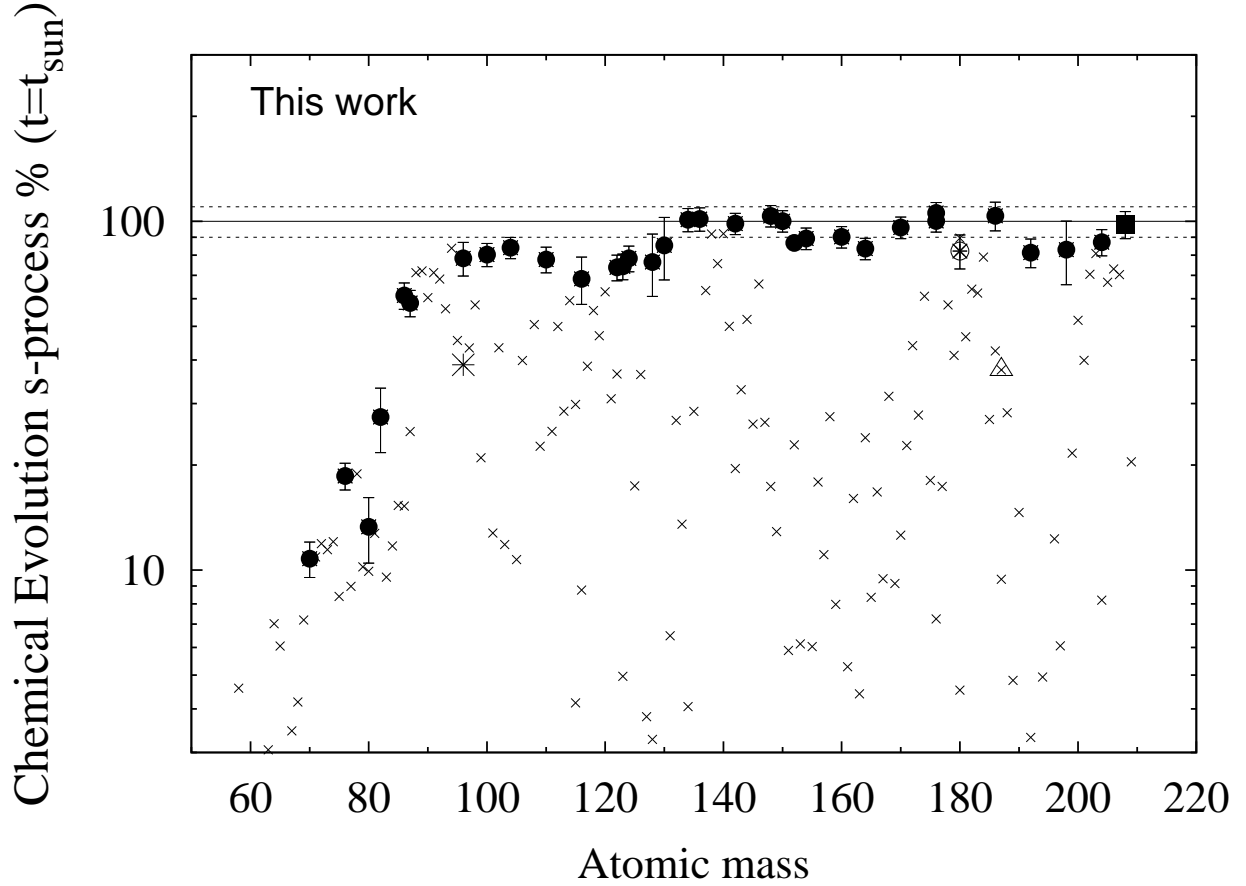


Fig. 2.— Reproduction of the solar s -process abundances (in %) obtained at the epoch of the solar system formation with GCE model. We display the updated solar s -process predictions presented in this work. The s -only isotopes are indicated by *filled circles*. Different symbols have been used for ^{180}Ta (*open circle*), ^{187}Os (*open triangle*), ^{208}Pb (*filled square*) and ^{96}Zr (*big asterisk*), see text. Errors account for solar abundance uncertainties. A full list of the solar s -process abundances is given in Table 1.

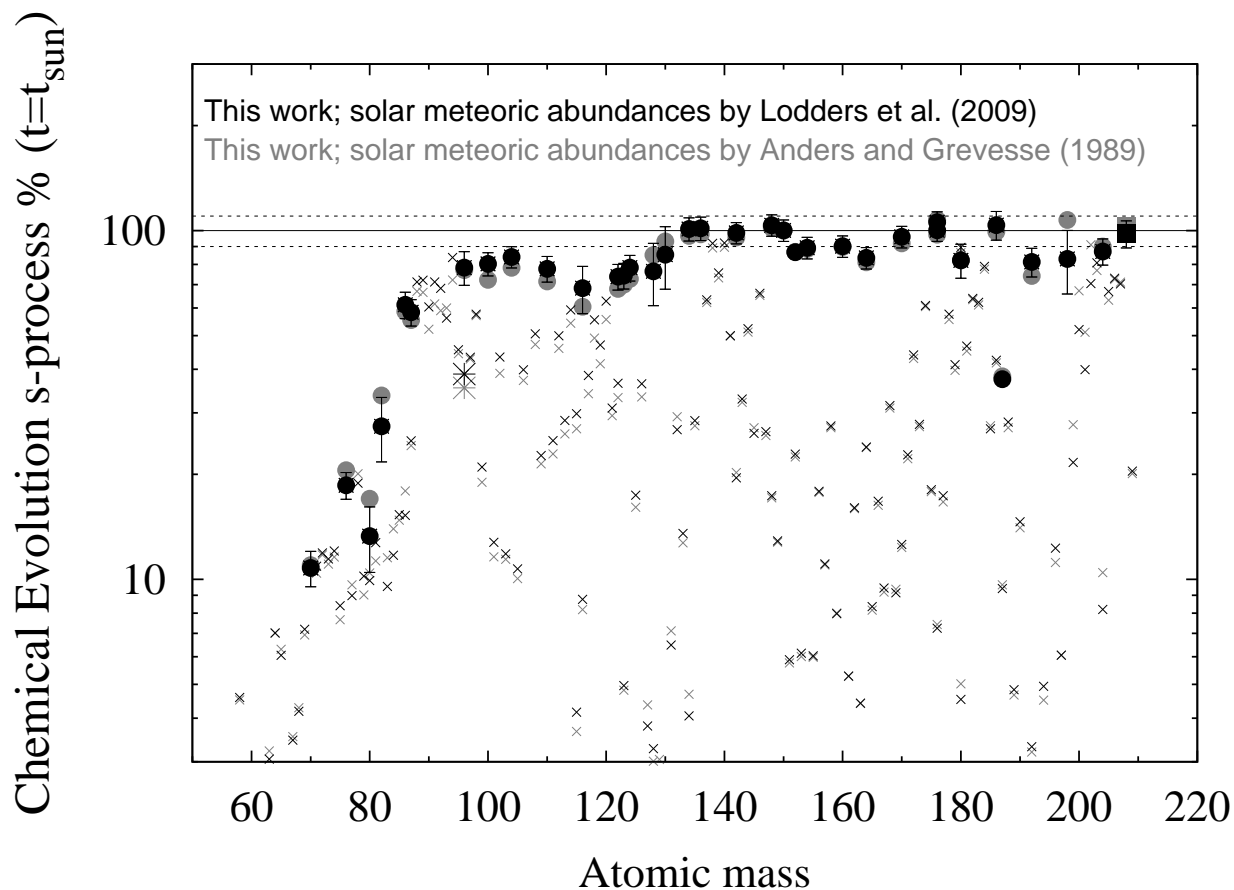


Fig. 3.— We compare updated solar s -process contribution (normalized to solar abundances by Lodders, Palme & Gail 2009; *black symbols*) with the same results normalized to solar abundances by Anders & Grevesse (1989) (*grey symbols*). The s -only isotopes are indicated by solid circles, ^{208}Pb by solid square and ^{96}Zr by big asterisk.

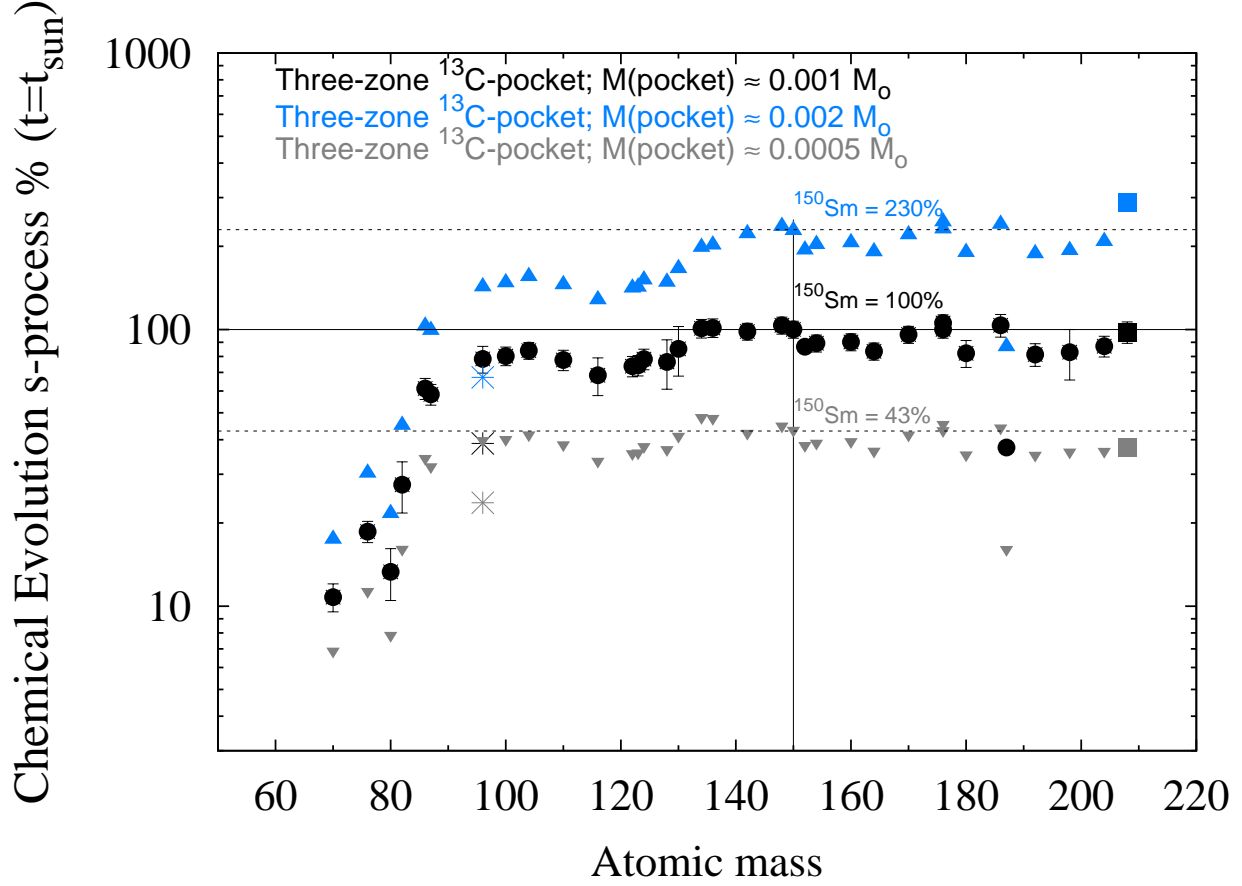


Fig. 4.— The s -only isotopes obtained with our standard three-zone ^{13}C -pocket choice are represented by *filled circles*; the tests with unchanged ^{13}C profile, but the mass of the pocket multiplied and divided by a factor of two are displayed with *filled triangles* and *down-rotated-triangles* (see text). GCE predictions obtained with $M(\text{pocket}) \sim 0.002 M_{\odot}$ are on average about a factor of 2 higher than solar (e.g., $^{150}\text{Sm} = 228\%$). On the other hand, solar s -abundances are halved with $M(\text{pocket}) \sim 0.0005 M_{\odot}$ (e.g., $^{150}\text{Sm} = 43\%$). These discrepancies could be solved once we change the weight of the different ^{13}C -pockets (see text). *See the electronic paper for a color version of this Figure.*

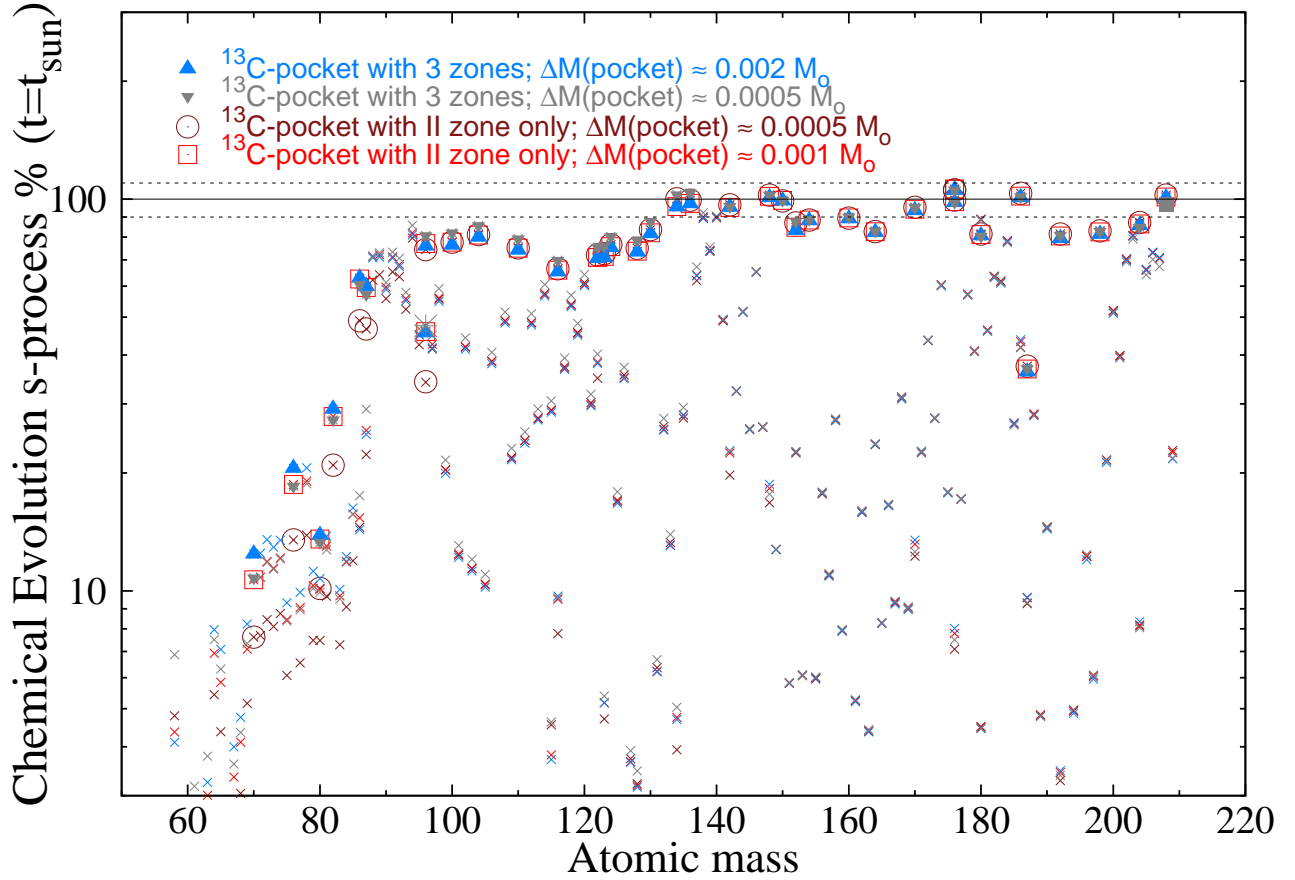


Fig. 5.— Effect of the ^{13}C -pocket uncertainties on solar s -process predictions computed with GCE model. The s -only isotopes obtained by several tests have been displayed with different symbols: the tests with unchanged ^{13}C profile, but the mass of the pocket multiplied and divided by a factor of two ($M(\text{pocket}) \sim 0.002$ and $0.0005 M_{\odot}$) are displayed with *filled triangles* and *down-rotated-triangles*. We provide two additional tests under the hypothesis that only the flat profile of zone II of our standard ^{13}C -pocket forms, and by assuming various mass size: $M(\text{pocket}) \sim 0.0005 M_{\odot}$ (*empty circles*) and $M(\text{pocket}) \sim 0.001 M_{\odot}$ (*empty squares*), which corresponds to the mass of zone II of our standard pocket multiplied by a factor of two. Results have to be compared with those obtained with our standard ^{13}C -pocket choice in Fig. 2. Note that, a different weighted range of ^{13}C -pocket strengths must be adopted in order to reproduce 100% of solar ^{150}Sm when changing the mass of the ^{13}C -pocket (see text). *See the electronic paper for a color version of this Figure.*

Table 1. Solar s -process contributions (in %) for isotopes from Kr to Bi obtained with GCE model. GCE results by Travaglio et al. (2004) ([T04]; normalised to solar meteoritic abundances by Anders & Grevesse 1989), are compared with updated GCE predictions ([This work]; normalised to solar meteoritic abundances by Lodders, Palme & Gail 2009). In columns 3 and 6 we report the percentages of the s -process solar contributions from LMS only; in columns 4 and 7 IMS s -process predictions are listed. The total s process contributions from AGB stars are reported in columns 5 and 8. Uncertainties refer to solar abundances by Anders & Grevesse (1989; column 5) and Lodders et al. (2009; column 8). In column 2, updated *main* – s contributions from Bisterzo et al. (2011) are also listed for comparison.

Isotope	Main-s ⁽¹⁾	Solar s -process distribution [T04]			Solar s -process distribution [This work]		
		LMS	IMS	(3)+(4)	LMS	IMS	(6)+(7)
(1)	(2)	(3)	(4)	(5)	(6)	(7)	(8)
⁸⁰ Kr	7.9	13.56	4.06	17.6	12.77	0.52	13.3
⁸² Kr	23.8	36.93	15.15	52.1	25.64	1.79	27.4
⁸³ Kr	9.0	12.28	4.85	17.1	8.92	0.62	9.5
⁸⁴ Kr	11.7	12.18	5.35	17.5	10.95	0.77	11.7
⁸⁶ Kr	16.2	21.49	33.96	55.4	11.65	3.58	15.2
Kr ⁽²⁾	13.4	16.66	11.31	28.0 ± 5.0	12.55	1.35	13.9 ± 2.9
⁸⁵ Rb	18.3	13.66	8.51	22.2	13.68	1.62	15.3
⁸⁷ Rb	29.3	27.33	49.50	76.8	17.94	6.99	24.9
Rb ⁽²⁾	21.5±1.5	17.65	20.47	38.1 ± 2.6	14.92	3.19	18.1 ± 1.6
⁸⁶ Sr ^(a)	59.2	43.17	8.42	51.6	59.29	1.85	61.1
⁸⁷ Sr	54.7	48.12	5.15	53.3	57.06	1.19	58.2
⁸⁸ Sr ^(a)	+6.0% ^(b)	64.26	9.60	73.9	69.83	1.31	71.1
Sr ⁽²⁾	97.3±6.8	60.70	9.13	69.8 ± 5.7	67.52	1.35	68.9 ± 5.9
⁸⁹ Y ^(a)	+3.0% ^(b)	60.89	7.43	68.3	70.64	1.29	71.9
Y ⁽²⁾	+3.0%±10.3 ^(b)	60.89	7.43	68.3 ± 4.2	70.64	1.29	71.9 ± 8.0
⁹⁰ Zr ^(a)	84.8	46.83	6.14	53.0	59.59	0.73	60.3
⁹¹ Zr	+5.5% ^(b)	61.49	17.62	79.1	69.52	1.64	71.2
⁹² Zr	+0.5% ^(b)	59.90	15.05	75.0	66.69	1.51	68.2
⁹⁴ Zr	+25.5% ^(b)	70.20	8.51	78.7	82.70	0.89	83.6
⁹⁶ Zr ^(a)	51.3	40.89	39.90	80.8	35.67	3.05	38.7

Table 1—Continued

Isotope	Main-s ⁽¹⁾	Solar <i>s</i> -process distribution [T04]			Solar <i>s</i> -process distribution [This work]		
	(2)	LMS (3)	IMS (4)	(3)+(4) (5)	LMS (6)	IMS (7)	(6)+(7) (8)
⁹³ Nb	85.6	54.65	11.49	66.1	54.93	1.09	56.0
Nb	85.6±8.6	54.65	11.49	66.1 ± 1.3	54.93	1.09	56.0 ± 6.3
⁹⁴ Mo ^(a)	0.9	0.59	0.00	0.6	0.95	0.00	1.0
⁹⁵ Mo	69.6	34.36	4.16	38.5	45.00	0.45	45.4
⁹⁶ Mo	+19.9% ^(b)	69.60	7.72	77.3	77.43	0.79	78.2
⁹⁷ Mo	63.7	39.60	5.74	45.3	42.77	0.51	43.3
⁹⁸ Mo	82.2	52.28	6.24	58.5	56.96	0.52	57.5
¹⁰⁰ Mo	4.5	1.98	0.40	2.4	2.27	0.03	2.3
Mo	57.7±5.8	33.85	4.06	37.9 ± 2.1	38.34	0.38	38.7 ± 4.3
⁹⁹ Ru	33.1	19.60	2.28	21.9	20.78	0.18	21.0
¹⁰⁰ Ru	+9.9% ^(b)	65.35	6.73	72.1	79.56	0.59	80.1
¹⁰¹ Ru	17.7	10.40	1.09	11.5	12.67	0.09	12.8
¹⁰² Ru	50.0	28.91	2.67	31.6	43.07	0.27	43.3
¹⁰⁴ Ru	2.5	1.49	0.10	1.6	1.44	0.01	1.4
Ru	37.3±2.2	21.91	2.19	24.1 ± 1.3	28.69	0.20	28.9 ± 2.3
¹⁰³ Rh	15.2	9.11	0.79	9.9	11.76	0.07	11.8
Rh	15.2±1.5	9.11	0.79	9.9 ± 0.8	11.76	0.07	11.8 ± 1.3
¹⁰⁴ Pd	+21.6% ^(b)	70.69	6.04	76.7	83.41	0.46	83.9
¹⁰⁵ Pd	15.7	9.11	0.79	9.9	10.64	0.06	10.7
¹⁰⁶ Pd	58.4	34.06	2.77	36.8	39.63	0.20	39.8
¹⁰⁸ Pd	74.6	43.37	3.27	46.6	50.27	0.24	50.5
¹¹⁰ Pd	3.0	1.88	0.20	2.1	1.62	0.01	1.6
Pd	53.1±2.7	30.91	2.50	33.4 ± 2.2	35.99	0.18	36.2 ± 2.6
¹⁰⁷ Ag	16.6	0.40	0.00	0.4	0.05	0.00	0.1

Table 1—Continued

Isotope	Main-s ⁽¹⁾	Solar <i>s</i> -process distribution [T04]			Solar <i>s</i> -process distribution [This work]		
	(2)	LMS	IMS	(3)+(4)	LMS	IMS	(6)+(7)
(1)	(2)	(3)	(4)	(5)	(6)	(7)	(8)
¹⁰⁹ Ag	28.1	16.73	1.29	18.0	22.50	0.11	22.6
Ag	22.1±1.1	8.26	0.62	8.9 ± 0.3	10.86	0.05	10.9 ± 0.8
¹⁰⁸ Cd ^(a)	0.4	0.20	0.00	0.2	1.12	0.00	1.1
¹¹⁰ Cd	+15.1% ^(b)	65.15	4.65	69.8	77.23	0.35	77.6
¹¹¹ Cd	38.0	15.84	1.09	16.9	24.83	0.11	24.9
¹¹² Cd	74.8	35.45	2.48	37.9	49.66	0.22	49.9
¹¹³ Cd	43.2	23.37	1.58	25.0	28.38	0.12	28.5
¹¹⁴ Cd	89.8	43.17	2.77	45.9	58.88	0.25	59.1
¹¹⁶ Cd	17.0	9.60	1.39	11.0	8.67	0.09	8.8
Cd	69.6±4.9	34.70	2.41	37.1 ± 2.5	45.85	0.20	46.1 ± 4.0
¹¹³ In ^(a)	0.0	0.00	0.00	0.0	0.01	0.00	0.0
¹¹⁵ In	44.3	24.75	1.58	26.3	29.69	0.12	29.8
In	42.4±3.0	23.69	1.52	25.2 ± 1.6	28.42	0.12	28.5 ± 2.5
¹¹⁴ Sn ^(a)	0.0	0.00	0.00	0.0	0.07	0.00	0.1
¹¹⁵ Sn ^(a)	2.8	2.08	0.00	2.1	4.16	0.00	4.2
¹¹⁶ Sn	96.2	59.60	3.47	63.1	68.00	0.27	68.3
¹¹⁷ Sn	56.9	33.37	1.98	35.3	38.21	0.15	38.4
¹¹⁸ Sn	80.6	50.89	2.97	53.9	55.13	0.22	55.4
¹¹⁹ Sn	65.3	27.52	1.58	29.1	46.72	0.19	46.9
¹²⁰ Sn	84.5	58.51	3.27	61.8	62.43	0.23	62.7
¹²² Sn	46.6	38.02	8.61	46.6	35.98	0.47	36.4
Sn	73.2±11.0	46.75	2.97	49.7 ± 4.7	52.27	0.22	52.5 ± 8.3
¹²¹ Sb	41.4	28.12	1.58	29.7	30.81	0.11	30.9
¹²³ Sb	6.5	4.75	0.99	5.7	4.91	0.05	5.0
Sb	26.4±4.0	18.12	1.33	19.5 ± 3.5	19.73	0.09	19.8 ± 3.1

Table 1—Continued

Isotope	Main-s ⁽¹⁾	Solar <i>s</i> -process distribution [T04]			Solar <i>s</i> -process distribution [This work]		
		LMS	IMS	(3)+(4)	LMS	IMS	(6)+(7)
(1)	(2)	(3)	(4)	(5)	(6)	(7)	(8)
¹²² Te	97.2	66.44	3.66	70.1	73.38	0.26	73.6
¹²³ Te	97.3	68.12	3.76	71.9	73.88	0.27	74.1
¹²⁴ Te	0.3% ^(b)	71.29	4.65	75.9	77.83	0.31	78.1
¹²⁵ Te	22.2	15.74	1.09	16.8	17.33	0.07	17.4
¹²⁶ Te	44.9	32.87	2.08	35.0	36.18	0.14	36.3
¹²⁸ Te	3.8	1.39	0.10	1.5	3.25	0.01	3.3
Te	19.6±1.4	13.57	0.86	14.4 ± 1.5	15.51	0.06	15.6 ± 1.3
¹²⁷ I	4.7	4.26	0.30	4.6	3.78	0.01	3.8
I	4.7±1.0	4.26	0.30	4.6 ± 1.0	3.78	0.01	3.8 ± 0.8
¹²⁸ Xe	81.1	66.83	4.16	71.0	76.01	0.28	76.3
¹²⁹ Xe	2.8	2.57	0.20	2.8	2.76	0.01	2.8
¹³⁰ Xe	88.1	68.81	4.16	73.0	84.83	0.29	85.1
¹³¹ Xe	6.7	5.35	0.30	5.6	6.46	0.02	6.5
¹³² Xe	27.1	28.42	1.58	30.0	26.76	0.08	26.8
¹³⁴ Xe	3.6	5.25	1.98	7.2	3.97	0.08	4.1
Xe	15.4	14.37	1.00	15.4 ± 3.1	15.03	0.06	15.1 ± 3.1
¹³³ Cs	15.6	12.28	0.69	13.0	13.48	0.04	13.5
Cs	15.6±0.8	12.28	0.69	13.0 ± 0.7	13.48	0.04	13.5 ± 1.0
¹³⁴ Ba	+12.5% ^(b)	88.22	4.16	92.4	+0.64 ^(b)	0.25	+0.9 ^(b)
¹³⁵ Ba	30.2	22.18	1.58	23.8	28.38	0.11	28.5
¹³⁶ Ba	+13.7% ^(b)	91.19	4.06	95.2	+1.04 ^(b)	0.27	+1.3 ^(b)
¹³⁷ Ba	67.3	62.28	9.41	71.7	62.63	0.58	63.2
¹³⁸ Ba	94.2	83.17	2.48	85.6	91.72	0.10	91.8
Ba	88.7±5.3	77.38	3.35	80.7 ± 5.2	85.03	0.17	85.2 ± 6.7

Table 1—Continued

Isotope	Main-s ⁽¹⁾	Solar <i>s</i> -process distribution [T04]			Solar <i>s</i> -process distribution [This work]				
	(1)	(2)	(3)	(4)	(3)+(4)	(5)	(6)	(7)	(8)
¹³⁹ La	71.0	60.79	1.68	62.5	75.40	0.07	75.5		
La	71.1±3.6	60.79	1.68	62.5 ± 1.5	75.40	0.07	75.5 ± 5.3		
¹⁴⁰ Ce	89.5	80.20	1.49	81.7	91.92	0.05	92.0		
¹⁴² Ce	19.3	23.76	2.77	26.5	19.46	0.07	19.5		
Ce	81.3±4.1	73.58	1.62	75.2 ± 1.6	83.47	0.05	83.5 ± 5.9		
¹⁴¹ Pr	51.7	46.83	0.89	47.7	49.86	0.03	49.9		
Pr	51.7±3.6	46.83	0.89	47.7 ± 1.3	49.86	0.03	49.9 ± 4.3		
¹⁴² Nd	97.6	89.31	0.99	90.3	98.31	0.04	98.3		
¹⁴³ Nd	32.7	30.89	0.69	31.6	32.84	0.02	32.9		
¹⁴⁴ Nd	52.2	49.41	1.19	50.6	52.19	0.03	52.2		
¹⁴⁵ Nd	26.3	26.73	0.69	27.4	26.15	0.02	26.2		
¹⁴⁶ Nd	65.5	62.38	1.58	64.0	65.98	0.04	66.0		
¹⁴⁸ Nd	19.2	15.15	0.59	15.7	17.33	0.01	17.3		
Nd	57.3±2.9	53.48	1.00	54.5 ± 1.0	57.51	0.03	57.5 ± 4.1		
¹⁴⁷ Sm	26.2	20.00	0.50	20.5	26.45	0.02	26.5		
¹⁴⁸ Sm	+2.2% ^(b)	97.13	2.48	99.6	+3.37 ^(b)	0.07	+3.4 ^(b)		
¹⁴⁹ Sm	12.6	12.18	0.30	12.5	12.87	0.01	12.9		
¹⁵⁰ Sm	100.0	97.13	2.77	99.9	99.93	0.07	100.0		
¹⁵² Sm	23.1	22.18	0.69	22.9	22.80	0.02	22.8		
¹⁵⁴ Sm	2.7	0.59	0.00	0.6	2.48	0.00	2.5		
Sm	31.3±1.6	28.83	0.78	29.6 ± 0.5	31.40	0.02	31.4 ± 2.2		
¹⁵¹ Eu	6.0	6.34	0.20	6.5	5.87	0.00	5.9		
¹⁵³ Eu	5.9	4.95	0.10	5.0	6.13	0.00	6.1		

Table 1—Continued

Isotope	Main-s ⁽¹⁾	Solar <i>s</i> -process distribution [T04]			Solar <i>s</i> -process distribution [This work]		
	(1)	LMS	IMS	(3)+(4)	LMS	IMS	(6)+(7)
	(2)	(3)	(4)	(5)	(6)	(7)	(8)
Eu	6.0±0.3	5.61	0.15	5.8 ± 0.1	6.01	0.00	6.0 ± 0.4
¹⁵² Gd ^(a)	70.5	85.74	1.49	87.2	86.55	0.04	86.6
¹⁵⁴ Gd	88.0	93.07	2.57	95.6	89.08	0.07	89.1
¹⁵⁵ Gd	5.7	5.74	0.20	5.9	6.02	0.00	6.0
¹⁵⁶ Gd	16.9	16.53	0.50	17.0	17.84	0.01	17.9
¹⁵⁷ Gd	10.6	10.40	0.30	10.7	11.05	0.01	11.1
¹⁵⁸ Gd	27.1	26.63	0.79	27.4	27.46	0.02	27.5
¹⁶⁰ Gd	0.6	0.98	0.00	1.0	0.69	0.00	0.7
Gd	13.5±0.7	14.89	0.43	15.3 ± 0.3	15.36	0.01	15.4 ± 1.1
¹⁵⁹ Tb	8.4	7.03	0.20	7.2	7.96	0.01	8.0
Tb	8.4±0.6	7.03	0.20	7.2 ± 0.2	7.96	0.01	8.0 ± 0.7
¹⁶⁰ Dy	91.3	98.12	3.07	+1.2 ^(b)	90.00	0.07	90.1
¹⁶¹ Dy	5.2	5.25	0.20	5.4	5.27	0.00	5.3
¹⁶² Dy	16.0	14.55	0.50	15.0	16.01	0.01	16.0
¹⁶³ Dy	4.3	3.47	0.10	3.6	4.41	0.00	4.4
¹⁶⁴ Dy	23.0	16.34	0.59	16.9	23.92	0.02	23.9
Dy	14.8±0.7	12.46	0.43	12.9 ± 0.2	15.03	0.01	15.0 ± 1.1
¹⁶⁵ Ho	8.1	7.43	0.20	7.6	8.34	0.01	8.3
Ho	8.1±0.6	7.43	0.20	7.6 ± 0.2	8.34	0.01	8.3 ± 0.7
¹⁶⁴ Er ^(a)	74.5	80.20	2.38	82.6	83.31	0.06	83.4
¹⁶⁶ Er	15.9	14.26	0.50	14.8	16.72	0.01	16.7
¹⁶⁷ Er	9.2	8.32	0.30	8.6	9.43	0.01	9.4
¹⁶⁸ Er	28.6	27.72	0.99	28.7	31.42	0.03	31.4
¹⁷⁰ Er	12.3	5.64	0.30	5.9	12.57	0.01	12.6

Table 1—Continued

Isotope	Main-s ⁽¹⁾	Solar <i>s</i> -process distribution [T04]			Solar <i>s</i> -process distribution [This work]		
	(1)	LMS	IMS	(3)+(4)	LMS	IMS	(6)+(7)
	(2)	(3)	(4)	(5)	(6)	(7)	(8)
Er	18.2±0.9	16.28	0.58	16.9 ± 0.3	19.44	0.02	19.5 ± 1.4
¹⁶⁹ Tm	12.2	12.97	0.50	13.5	9.13	0.01	9.1
Tm	12.2±0.9	12.97	0.50	13.5 ± 0.4	9.13	0.01	9.1 ± 0.8
¹⁷⁰ Yb	90.6	100.00	3.17	+3.2 ^(b)	95.77	0.07	95.8
¹⁷¹ Yb	20.9	13.47	0.50	14.0	22.70	0.02	22.7
¹⁷² Yb	43.9	29.31	0.99	30.3	43.88	0.04	43.9
¹⁷³ Yb	26.9	20.69	0.69	21.4	27.77	0.02	27.8
¹⁷⁴ Yb	60.5	48.02	1.68	49.7	60.81	0.05	60.9
¹⁷⁶ Yb	8.2	10.50	0.69	11.2	7.23	0.01	7.2
Yb	39.9±2.0	31.31	1.12	32.4 ± 0.7	40.46	0.03	40.5 ± 2.9
¹⁷⁵ Lu	17.8	17.13	0.59	17.7	18.04	0.02	18.1
¹⁷⁶ Lu	+1.2% ^(b)	+33.66 ^(b)	3.96	+37.6 ^(b)	+5.40 ^(b)	0.12	+5.54 ^(b)
Lu	20.2±1.0	20.42	0.69	21.1 ± 0.4	20.50	0.02	20.5 ± 1.5
¹⁷⁶ Hf	97.3	93.37	3.07	96.4	+0.03 ^(b)	0.07	+0.13 ^(b)
¹⁷⁷ Hf	17.2	17.72	0.69	18.4	17.33	0.01	17.3
¹⁷⁸ Hf	58.5	55.05	1.98	57.0	57.46	0.05	57.5
¹⁷⁹ Hf	41.0	35.54	1.29	36.8	41.15	0.04	41.2
¹⁸⁰ Hf	88.8	73.07	2.77	75.8	89.29	0.08	89.4
Hf	61.0±3.1	53.68	1.98	55.7 ± 1.3	61.07	0.05	61.1 ± 4.3
¹⁸⁰ Ta ^{m(a)}	75.5	46.93	1.49	48.4	81.99	0.05	82.0
¹⁸¹ Ta	46.5	40.00	1.51	41.5	46.52	0.04	46.6
Ta	46.5±4.7	40.00	1.51	41.5 ± 0.9	46.52	0.04	46.6 ± 5.2
¹⁸⁰ W ^(a)	5.1	4.65	0.10	4.8	4.52	0.00	4.5

Table 1—Continued

Isotope	Main-s ⁽¹⁾	Solar <i>s</i> -process distribution [T04]			Solar <i>s</i> -process distribution [This work]		
		LMS	IMS	(3)+(4)	LMS	IMS	(6)+(7)
(1)	(2)	(3)	(4)	(5)	(6)	(7)	(8)
¹⁸² W	60.6	45.45	1.58	47.0	63.75	0.06	63.8
¹⁸³ W	57.9	53.07	1.98	55.0	62.13	0.06	62.2
¹⁸⁴ W	77.8	68.22	2.48	70.7	78.75	0.07	78.8
¹⁸⁶ W	58.5	44.85	1.98	46.8	42.36	0.05	42.4
W	64.8±6.5	53.30	2.02	55.3 ± 2.9	61.96	0.06	62.0 ± 6.9
¹⁸⁵ Re	27.4	23.86	0.89	24.8	26.96	0.02	27.0
¹⁸⁷ Re	10.0	8.42	0.10	8.5	9.38	0.01	9.4
Re	16.2±1.6	13.92	0.38	14.3 ± 1.4	15.65	0.02	15.7 ± 1.8
¹⁸⁶ Os	+11.6% ^(b)	97.52	3.17	+0.7 ^(b)	+3.37 ^(b)	0.09	+3.53 ^(b)
¹⁸⁷ Os	39.9	42.28	2.67	45.0	37.40	0.03	37.4
¹⁸⁸ Os	29.6	18.51	0.69	19.2	28.17	0.03	28.2
¹⁸⁹ Os	4.5	4.16	0.20	4.4	4.81	0.01	4.8
¹⁹⁰ Os	14.6	11.58	0.50	12.1	14.59	0.02	14.6
¹⁹² Os	3.5	0.89	0.00	0.9	3.30	0.00	3.3
Os	12.3±1.0	8.67	0.34	9.0 ± 0.6	11.88	0.01	11.9 ± 1.1
¹⁹¹ Ir	2.0	1.78	0.10	1.9	1.92	0.00	1.9
¹⁹³ Ir	1.3	0.99	0.00	1.0	1.42	0.00	1.4
Ir	1.6±0.1	1.29	0.04	1.3 ± 0.1	1.60	0.00	1.6 ± 0.1
¹⁹² Pt	87.1	98.22	3.37	+1.6 ^(b)	81.08	0.08	81.2
¹⁹⁴ Pt	6.6	3.86	0.10	4.0	4.93	0.01	4.9
¹⁹⁵ Pt	2.6	1.58	0.10	1.7	2.00	0.00	2.0
¹⁹⁶ Pt	13.2	9.41	0.30	9.7	12.26	0.01	12.3
¹⁹⁸ Pt	0.0	0.00	0.00	0.0	0.09	0.00	0.1
Pt	7.1±0.6	4.95	0.17	5.1 ± 0.4	6.04	0.01	6.0 ± 0.6

Table 1—Continued

Isotope	Main-s ⁽¹⁾	Solar <i>s</i> -process distribution [T04]			Solar <i>s</i> -process distribution [This work]				
	(1)	(2)	(3)	(4)	(3)+(4)	(5)	(6)	(7)	(8)
¹⁹⁷ Au	5.9	5.64	0.20	5.8	6.05	0.01	6.1		
Au	5.9±0.6	5.64	0.20	5.8 ± 0.9	6.05	0.01	6.1 ± 0.7		
¹⁹⁸ Hg	82.6	100.00	3.37	+3.4 ^(b)	82.70	0.09	82.8		
¹⁹⁹ Hg	21.7	25.84	0.89	26.7	21.59	0.02	21.6		
²⁰⁰ Hg	52.4	62.77	1.98	64.8	51.89	0.05	51.9		
²⁰¹ Hg	39.7	47.13	1.49	48.6	39.83	0.04	39.9		
²⁰² Hg	65.3	78.02	2.28	80.3	70.33	0.08	70.4		
²⁰⁴ Hg	8.0	9.21	0.00	9.2	8.18	0.01	8.2		
Hg	49.3±9.9	58.97	1.82	60.8 ± 7.3	50.69	0.05	50.7 ± 10.5		
²⁰³ Tl	83.1	72.08	2.18	74.3	80.57	0.09	80.7		
²⁰⁵ Tl	62.8	75.15	1.98	77.1	66.69	0.06	66.7		
Tl	68.8±5.5	74.24	2.04	76.3 ± 7.2	70.79	0.07	70.9 ± 6.7		
²⁰⁴ Pb	96.7	92.87	2.57	95.4	86.85	0.10	87.0		
²⁰⁶ Pb	66.6	61.88	1.39	63.3	72.87	0.07	72.9		
²⁰⁷ Pb	57.8	80.00	1.39	81.4	70.13	0.05	70.2		
²⁰⁸ Pb	41.6	92.67	1.19	93.9	97.70	0.04	97.7		
Pb	50.7±3.6	84.35	1.29	85.6 ± 6.8	87.20	0.05	87.2 ± 7.5		
²⁰⁹ Bi	6.3	18.22	0.59	18.8	20.37	0.03	20.4		
Bi	6.3±0.6	18.22	0.59	18.8 ± 1.6	20.37	0.03	20.4 ± 2.1		

⁽¹⁾The *main* – *s* component is reproduced as an average between AGB models of $M = 1.5$ and $3 M_{\odot}$ and half solar metallicity, as in Arlandini et al. (1999). Values are taken from Bisterzo et al. (2011).

⁽²⁾Note that massive stars may produce a consistent amount of Sr-Y-Zr, and in minor quantity up to Te-Xe (Pignatari et al. 2010, 2013).

^(a)Isotopes that receive an additional contribution from p -process (Travaglio et al. 2011).

^(b)Overabundances with respect to solar (in percentage).

Table 2. Internal structure of the ^{13}C -pockets adopted in the tests displayed in Fig. 5. First, we specify the mass and the amount of ^{13}C and ^{14}N in the three-zone ^{13}C -pocket adopted so far (case ST with zones I-II-III; $M(\text{pocket}) = 1.09\text{E}-3 M_{\odot}$; represented with *filled circles*). In *TEST A* and *B* we leave the ^{13}C profile unchanged, but we multiply and divide by a factor of two the mass of the pocket ($M(\text{pocket}) = 2 \times 1.09\text{E}-3 M_{\odot}$; displayed with *filled triangles*; $M(\text{pocket}) = 0.5 \times 1.09\text{E}-3 M_{\odot}$; displayed with *filled down-rotated-triangles*). Under the hypothesis that only the flat profile of zone II of our standard ^{13}C -pocket forms (zone-II model, with flat $X(^{13}\text{C})$ and $X(^{14}\text{N})$ abundances), we provide two additional tests in which we change the mass involved in the pocket: *TEST C* with $M(\text{pocket}) = 5.30\text{E}-4 M_{\odot}$ (*empty circles*) and *TEST D* with $M(\text{pocket}) = 2 \times 5.30\text{E}-4 M_{\odot}$ (*empty squares*).

	zone I	zone II	zone III
Three-zone model with $M(\text{pocket}) = 1.09\text{E}-3 M_{\odot}$			
Mass(M_{\odot})	5.50E-4	5.30E-4	7.50E-6
$X(^{13}\text{C})$	3.20E-3	6.80E-3	1.60E-2
$X(^{14}\text{N})$	1.07E-4	2.08E-4	2.08E-3
<i>TEST A</i> : three-zone model with $M(\text{pocket}) = 2 \times 1.09\text{E}-3 M_{\odot}$			
Mass(M_{\odot})	1.10E-3	1.06E-3	1.50E-5
$X(^{13}\text{C})$	3.20E-3	6.80E-3	1.60E-2
$X(^{14}\text{N})$	1.07E-4	2.08E-4	2.08E-3
<i>TEST B</i> : zone-II model with $M(\text{pocket}) = 0.5 \times 1.09\text{E}-3 M_{\odot}$			
Mass(M_{\odot})	2.75E-4	2.65E-4	3.75E-6
$X(^{13}\text{C})$	3.20E-3	6.80E-3	1.60E-2
$X(^{14}\text{N})$	1.07E-4	2.08E-4	2.08E-3
<i>TEST C</i> : zone-II model with $M(\text{pocket}) = 5.30\text{E}-4 M_{\odot}$			
Mass(M_{\odot})	–	5.30E-4	–
$X(^{13}\text{C})$	–	6.80E-3	–
$X(^{14}\text{N})$	–	2.08E-4	–
<i>TEST D</i> : zone-II model with $M(\text{pocket}) = 2 \times 5.30\text{E}-4 M_{\odot}$			
Mass(M_{\odot})	–	1.06E-3	–
$X(^{13}\text{C})$	–	6.80E-3	–
$X(^{14}\text{N})$	–	2.08E-4	–

